NANO · MICRO small
www.small-journal.com

Extending the Colloidal Transition Metal Dichalcogenide Library to ReS_2 Nanosheets for Application in Gas Sensing and Electrocatalysis

Beatriz Martín-García, Davide Spirito, Sebastiano Bellani, Mirko Prato, Valentino Romano, Anatolii Polovitsyn, Rosaria Brescia, Reinier Oropesa-Nuñez, Leyla Najafi, Alberto Ansaldo, Giovanna D'Angelo, Vittorio Pellegrini, Roman Krahne, Iwan Moreels,* and Francesco Bonaccorso**

Among the large family of transition metal dichalcogenides, recently ReS_2 has stood out due to its nearly layer-independent optoelectronic and physicochemical properties related to its 1T distorted octahedral structure. This structure leads to strong in-plane anisotropy, and the presence of active sites at its surface makes ReS_2 interesting for gas sensing and catalysts applications. However, current fabrication methods use chemical or physical vapor deposition (CVD or PVD) processes that are costly, time-consuming and complex, therefore limiting its large-scale production and exploitation. To address this issue, a colloidal synthesis approach is developed, which allows the production of ReS_2 at temperatures below 360 °C and with reaction times shorter than 2h. By combining the solution-based synthesis with surface functionalization strategies, the feasibility of colloidal ReS_2 nanosheet films for sensing different gases is demonstrated with highly competitive performance in comparison with devices built with CVD-grown ReS_2 and MoS_2. In addition, the integration of the ReS_2 nanosheet films in assemblies together with carbon nanotubes allows to fabricate electrodes for electrocatalysis for H_2 production in both acid and alkaline conditions. Results from proof-of-principle devices show an electrocatalytic overpotential competitive with devices based on ReS_2 produced by CVD, and even with MoS_2, WS_2, and $MoSe_2$ electrocatalysts.

1. Introduction

Transition metal dichalcogenides (TMDCs) are highly interesting and versatile materials due to their physicochemical properties that can be modified by exfoliation into single- or few-layer structures.[1–4] Due to quantum confinement and/or surface effects, such single and few-layer structures can behave differently from their bulk phase and manifest photoluminescence,[5] catalytically active sites,[6] or strong light–matter coupling.[7] Moreover, depending on their composition and structure, they can be semiconductors (e.g., MoS_2, WS_2), metals (e.g., NbS_2, VSe_2), or even superconductors (e.g., $NbSe_2$, TaS_2).[1,8] Among the TMDCs, rhenium disulfide (ReS_2) has recently emerged as an interesting material.[9–11] In contrast to the well-known group-VI_B TMDCs (MoS_2 or WS_2), which present a hexagonal crystalline structure, ReS_2 has an unusual distorted octahedral (1T) triclinic structure,

Dr. B. Martín-García, Dr. S. Bellani, V. Romano, Dr. L. Najafi, Dr. A. Ansaldo, Dr. V. Pellegrini, Dr. F. Bonaccorso
Graphene Labs
Istituto Italiano di Tecnologia
via Morego 30, 16163 Genova, Italy
E-mail: beatriz.martin-garcia@iit.it; francesco.bonaccorso@iit.it

Dr. B. Martín-García, Dr. A. Polovitsyn, Prof. I. Moreels
Nanochemistry Department
Istituto Italiano di Tecnologia
via Morego 30, 16163 Genova, Italy

The ORCID identification number(s) for the author(s) of this article can be found under https://doi.org/10.1002/smll.201904670.

DOI: 10.1002/smll.201904670

Dr. D. Spirito, Dr. R. Krahne
Optoelectronics Group
Istituto Italiano di Tecnologia
via Morego 30, 16163 Genova, Italy

Dr. M. Prato
Materials Characterization Facility
Istituto Italiano di Tecnologia
via Morego 30, 16163 Genova, Italy

V. Romano, Prof. G. D'Angelo
Dipartimento di Scienze Matematiche ed Informatiche
Scienze Fisiche e Scienze della Terra
Università di Messina
Viale F. Stagno d'Alcontres 31, S. Agata 98166, Messina, Italy

Dr. A. Polovitsyn, Prof. I. Moreels
Department of Chemistry
Ghent University
Krijgslaan 281-S3, 9000 Gent, Belgium
E-mail: iwan.moreels@ugent.be

Dr. R. Brescia
Electron Microscopy Facility
Istituto Italiano di Tecnologia
via Morego 30, 16163 Genova, Italy

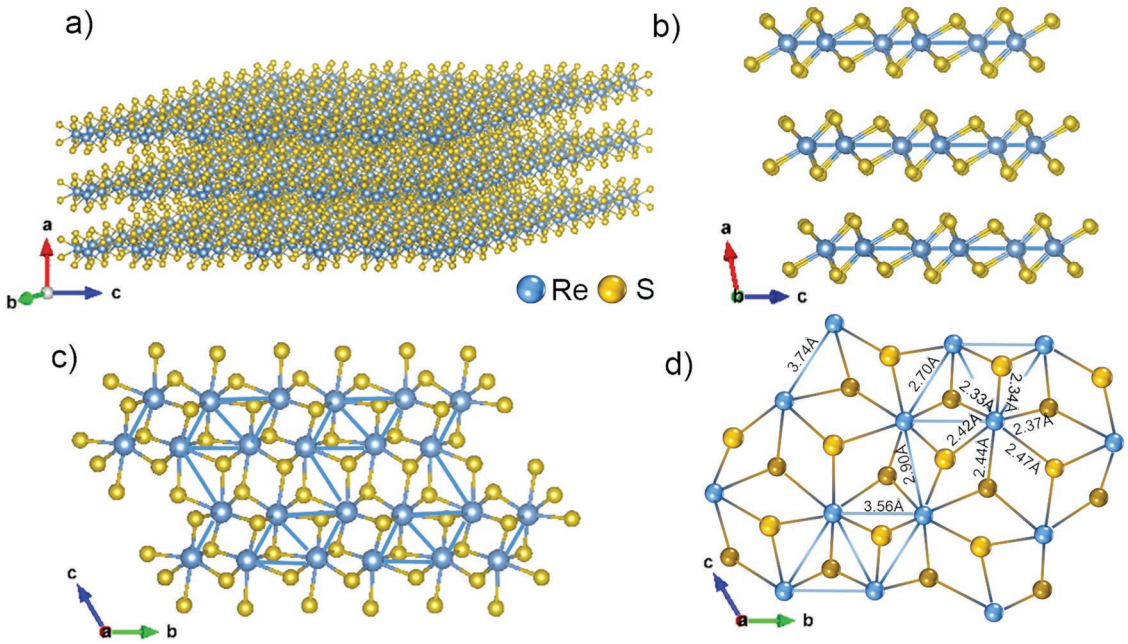

Scheme 1. Sketches of the distorted 1T crystal structure of the ReS_2 from different perspectives. Lattice orientations are indicated by the *a–b–c* axes. a) A general view of a three-layer system, b) side view of the layers, c) top view of the three layer crystals where the Re_4 clusters can be identified, d) enlarged top view indicating the distances between the atoms. To obtain the crystal structure we used the crystallographic data from Murray et al. and Kelty et al.[12,13] and the VESTA v.3.4.6 software.[14]

leading to a strong in-plane anisotropy like black phosphorous (BP).[9,10] However, unlike BP, ReS_2 is stable in air.[9,10] The ReS_2 structure consists of a $P\bar{1}$ symmetry with Re atoms forming Re_4 clusters, interconnected in zig-zag chains, and distorted S_6 octahedra that are formed upon cooperative atomic displacement (**Scheme 1**).[9,11–13]

Moreover, ReS_2 exhibits both metal—chalcogen and metal—metal bonds due to the extra valence electron of Re atoms, since Re belongs to the group-VII of elements.[9,11–13] This structural anisotropy translates to electrical, optical, vibrational,[15] thermal,[16] and physicochemical properties that do not depend significantly on the number of layers. For example, ReS_2 is a direct-gap semiconductor (1.4–1.5 eV) from bulk to monolayer (0.7 nm) thicknesses,[15] unlike MoS_2 or WS_2 that instead present an indirect to direct bandgap (E_g) transition when the thickness is reduced from bulk to a monolayer.[9,10] The predictability of the physical properties of ReS_2 has made it attractive for a large variety of applications, in which it can be integrated as monolayer or few-layer crystals in polarization-sensitive photodetectors,[17–19] field effect or heterojunction transistor structures,[20,21] and gas sensors,[25,26] or as thick nanocrystals or nanocrystal sheets with some tens up to hundred layers in batteries,[24–26] solar cells,[27] and electrocatalysts.[28,29]

Despite its favorable properties, the feasibility of ReS_2 in technological and economic terms will strongly depend on the development of a scalable synthesis that can be readily integrated with the current device technology, being compatible with economic constrictions. In this regard, there are several challenges. First, Re is not an earth-abundant element, and therefore, its price (around 2800 € kg^{-1}[30]), determined by its availability and the market demand, is high in comparison to representative TMDCs, such as Mo and W (less than 30 € kg^{-1}[31]). Moreover, current methods for the production of ReS_2 are mainly based on chemical vapor deposition[19,32–34] (CVD), epitaxial growth,[35] and the Bridgman method,[20] and rely on high process temperatures (from 450 to 1100 °C) for the precursor decomposition (e.g., the melting points of Re powder 3180 °C; Re–Te eutectoid 430 °C; ReO_3 400 °C).[9,10] Moreover, they also imply the use of halogen vapor transport in the case of CVD;[32] or HF treatments for cleaning in the Bridgman method[20] and as etchant to delaminate the ReS_2 from the mica substrate in the epitaxial growth.[35] In addition, the aforementioned methods require long processing times from several hours for CVD[9,10] and epitaxial growth[9,10] up to several weeks for the Bridgman method.[9,10,20] Solution-based techniques, such as chemical-intercalation[36] and liquid phase exfoliation (LPE),[37,38] have been developed as large-scale routes for the ReS_2 flakes production, but in most cases CVD-grown ReS_2 is used as starting material, and therefore these methodologies inevitably still rely on expensive and demanding processing. To face the challenges related to the fabrication of ReS_2, colloidal synthesis can be an alternative method for its large-scale production,[39–41] achieving a compromise between crystal quality and physical properties that are needed for device applications. In fact, colloidal synthesis has already been successful in the development of other TMDCs, such as MoS_2,[2,42–45]

Dr. R. Oropesa-Nuñez, Dr. F. Bonaccorso, Dr. V. Pellegrini
BeDimensional Spa.
Via Albisola 121, 16163 Genova, Italy

$MoSe_2$,[2,46,47] $MoTe_2$,[48] WS_2,[49] WSe_2,[46] ZrS_2,[50] TiS_2,[50] and HfS_2.[50]

Transition metal dichalcogenides have already been explored as gas sensing materials showing high sensitivity, room temperature operation, facile processing, and high resistance to degradation, in order to address the main drawbacks of the materials that are currently used in environmental monitoring such as metal oxides,[51] conducting polymers,[51] and carbon nanotubes.[51] Recently, an interest in the use of ReS_2 for the fabrication of gas sensors[22,23] has emerged due to its strong interaction with nonmetal adatoms (H, N, P, O, S, F, etc.). In transistors built from Scotch-tape exfoliated ReS_2,[22] a key role of the sulfur vacancies and interlayer interactions has been demonstrated to enhance the gas sensing capabilities, leading, for example, to better performance than MoS_2.[52] and graphene-based detectors[53] for NH_3 detection. In addition, ReS_2 is also sensitive to other gases such as O_2 or air, and can be applied in humidity sensors.[23]

The presence of active sites at the surface, promoted by the stable and distorted 1T structure of the ReS_2, can be beneficial not only for the gas sensing applications but also in electrocatalysis for the molecular hydrogen (H_2) production from electrochemical water splitting,[25,36,54] an important and growing field due to the high energy density of ≈120–140 MJ kg^{-1} and sustainability of H_2.[55–57] Actually, before ReS_2, other TMDCs have been reported as high-performance hydrogen evolution reaction (HER)-electrocatalysts.[6,58–60] In particular, the group-VI_B TMDCs have reached an advanced stage of development,[6,58–60] exhibiting overpotentials inferior to 0.1 V at a cathodic current density of 10 mA cm^{-2} (η_{10}) in both acid[61,62] and alkaline[63–65] media. However, only the metallic edge states of their trigonal prismatic (2H) phase can absorb H^+ with a small Gibbs free energy ($\Delta G_H{}^0 \approx 0.08$ eV for MoS_2), acting as active site for HER,[66–68] while the basal planes are electrocatalytically inactive.[67–69] Recent advances have shown that the HER activity of group-VI_B TMDCs can be significantly enhanced when the semiconducting 2H phase of MoS_2 is converted into metallic 1T (octahedral) phase.[70,71] In this context, the stable and distorted 1T structure of the ReS_2 represents an interesting electrocatalyst model, which can be advantageous compared to group-VI_B TMDCs due to its metal−metal bonds. These bonds create a superlattice structure of Re chains that distort the octahedral structure of 1T phase (C_{3v} symmetry).[15,28] Consequently, the Gibbs free energy of the hydrogen adsorption ($\Delta G_H{}^0$) on ReS_2 basal planes can be as low as ≈0.1 eV.[28] In fact, recent theoretical and experimental studies have shown that Re−Re bonds serve as electron reservoirs to originate an intrinsic charge distribution regulation, which tunes the Gibbs free energy of the hydrogen adsorption ($\Delta G_H{}^0$) on ReS_2 basal planes towards the optimal thermoneutral value (i.e., 0 eV).[54] This value is comparable to that of metallic edge states of 2H-MoS_2 (≈0.08 eV).[28,72] However, thanks to the HER-activity of its basal planes, the ReS_2 should exhibit a higher number of active sites than group-VI_B TMDCs.[28] In addition, in TMDCs such as MoS_2 or WS_2, the HER-activity strongly depends on the number of layers due to the dependence with the E_g, and the HER-activity weakens by passing from monolayer to few-layer materials as a consequence of an inefficient intra-flake electron transport via a hopping mechanism.[6,69] In contrast, the nearly layer-independent properties of ReS_2 make it a suitable catalyst, either monolayer or multilayer structures,[9,15] as it has been demonstrated in 3D structures composed by multilayer (≥17L) ReS_2 flakes.[28,29]

In this work, we report a colloidal approach for the synthesis of ReS_2 nanosheets, starting from $ReCl_5$ and elemental sulfur as precursors. The obtained ReS_2 sheets are tested as active material in gas sensors and HER. For the colloidal synthesis of the ReS_2 nanosheets, we use elemental sulfur instead of CS_2[42,49,50] or dodecanethiol (DDT)[43,50] that are used as sulfur source for the colloidal synthesis of other TMDCs.[42,43,49,50] The advantage of using elemental sulfur relies on the fact that it is much less hazardous and/or toxic than the aforementioned precursors. We compare the properties of the colloidal ReS_2 with their bulk and LPE counterparts, and find that the colloidal ReS_2 nanosheets have a similar composition and E_g, but lower crystallinity. We fabricated gas sensors for a variety of agents by electrically contacting homogenous films of colloidal ReS_2 nanosheets. With suitable ligands for the surface functionalization of the colloidal ReS_2 nanosheets, we are able to enhance the gas sensor sensitivity to toxic gases (NH_3) and humidity, compared to their nonfunctionalized counterparts. Sensitivity, recovery and time response of the functionalized gas sensors based on colloidal ReS_2 nanosheets can compete with gas sensors fabricated from CVD-produced ReS_2 reported in literature.[23] Concerning the HER activity in acidic media, a mixture of colloidally synthesized ReS_2 in combination with carbon nanotubes, resulted in electrodes that can compete with the state-of-art CVD (KI)-aided ReS_2.[54]

2. Results and Discussion

The colloidal ReS_2 nanosheets were synthesized from $ReCl_5$ and elemental sulfur by a syringe pump method,[42,44,47–49] in which the Re-precursor is added dropwise in a S-oleylamine (S-OlAm) solution at 350 °C. This procedure follows the use of chloride metal precursors[42,48–50] and the progressive injection method[42,44,47–49] for the colloidal synthesis of TMDCs, but it introduces elemental S as the sulfur source. The chalcogen source can play a role in the growth kinetics, in particular in the formation of H_2S. Cheon's group demonstrated that sudden H_2S influx, triggered by CS_2, favors the formation of nanodisks, while continuous H_2S formation with DDT leads to flakes.[50] With elemental sulfur as chalcogen source we obtained nanosheets, and therefore assume slow H_2S kinetics in the oleylamine medium, with a release of ≈75% over a 3 h heating period.[73] For the nucleation and growth of the nanosheets, we added the $ReCl_5$-oleic acid (OA) precursor dropwise, with a syringe pump, to the hot solution. High-angle annular dark-field scanning transmission electron microscopy (HAADF-STEM) images in **Figure 1**a,b (see also Figure S1a in the Supporting Information) show the formation of colloidal ReS_2 nanosheets (hereafter, c-ReS_2) with variable dimensions, formed by individual domains with a lateral size of ≈4 ± 1 nm. Moreover, some c-ReS_2 nanosheets are found lying perpendicular to the support film (Figure 1c,d). From these images a thickness of ≈0.4 ± 0.1 nm is estimated for individual c-ReS_2 nanosheets. This value is lower than the 0.7 nm reported for mechanically exfoliated monolayers in ReS_2.[15] The discrepancy can be

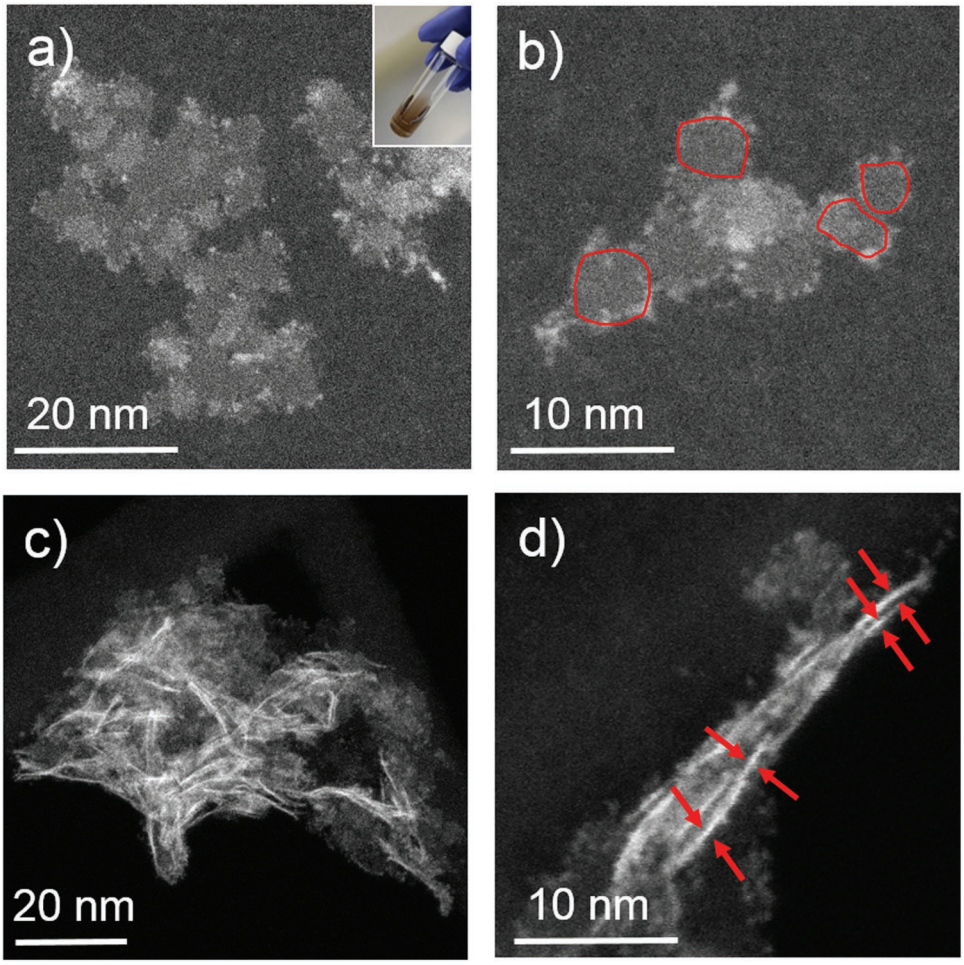

Figure 1. Representative HAADF-STEM images of the c-ReS_2 nanosheets, showing a,b) nanosheets lying mainly parallel to the support film, with individual domains highlighted in (b). In c,d) the nanosheets lie mainly perpendicular to the carbon support film, as clarified in (d) by arrows pointing at nanosheets viewed along their side. The inset in (a) shows a photograph of the c-ReS_2 dispersion in toluene.

attributed to the heavy strain building up in these highly anisotropic colloidal 2D structures, leading to in-plane expansion of the lattice and contraction along the out-of-plane direction.[74] The obtained c-ReS_2 nanosheets are comparable in morphology to other colloidal TMDC materials such as MoS_2,[42,43,45] WS_2,[50] or WSe_2[46] reported in literature. The ReS_2 sheets prepared by LPE (hereafter named LPE-ReS_2), as control material, do not show aggregation as demonstrated in Figure S2a,b in the Supporting Information. Regarding the nanosheet formation, previous studies on the CVD production of ReS_2 proved that there are two growth mechanisms: a fast one in (100) direction, and a slow one in (020) direction. To obtain nanosheets with a 1T distorted octahedral structure, the growth rate in both (100) and (020) directions should be comparable,[19] which may be achieved by oleic acid, oleylamine and Cl^- (from the $ReCl_5$) acting as ligands that passivate different crystal facets. In order to gain insight into the crystal structure, we compare the selected-area electron diffraction (SAED) patterns from c-ReS_2 nanosheets and LPE-ReS_2 flakes showing comparable 2θ values for Bragg peak positions (see Figure S3 in the Supporting Information for the TEM-SAED patterns), which correspond to the 1T distorted octahedral structure. Furthermore, broader diffraction features characterize the c-ReS_2 nanosheets, due to the much smaller size of single-crystal domains (few nm or less in the colloidal sample vs hundreds of nm for LPE flakes).

The composition of the as-prepared c-ReS_2 was investigated by X-Ray photoelectron spectroscopy (XPS), as shown in **Figure 2**a,b, revealing an atomic stoichiometry Re:S of 1:1.3, which is estimated from the Re 4f and S 2p spectra. This ratio is slightly smaller than the one expected from the 1:2 ReS_2 stoichiometry. However, also the LPE fabricated samples and bulk ReS_2 yield lower Re:S stoichiometric values of around 1:1.6 and 1:1.7, respectively (see also Figure S1e in the Supporting Information for complementary elemental analysis). It is interesting to note that in the LPE and bulk cases, the S 2p signal can be decomposed in two different doublets, corresponding to two different chemical environments of sulfur. Similar results have been reported by Dalmatova et al.,[75] and the two S components have been assigned to ReS_2 (doublet at lower binding energy, with S $2p_{3/2}$ component at ≈161.4 eV) and to S atoms that are not connected to Re atoms (doublet at higher binding energy, with S $2p_{3/2}$ component at ≈162.1 eV).

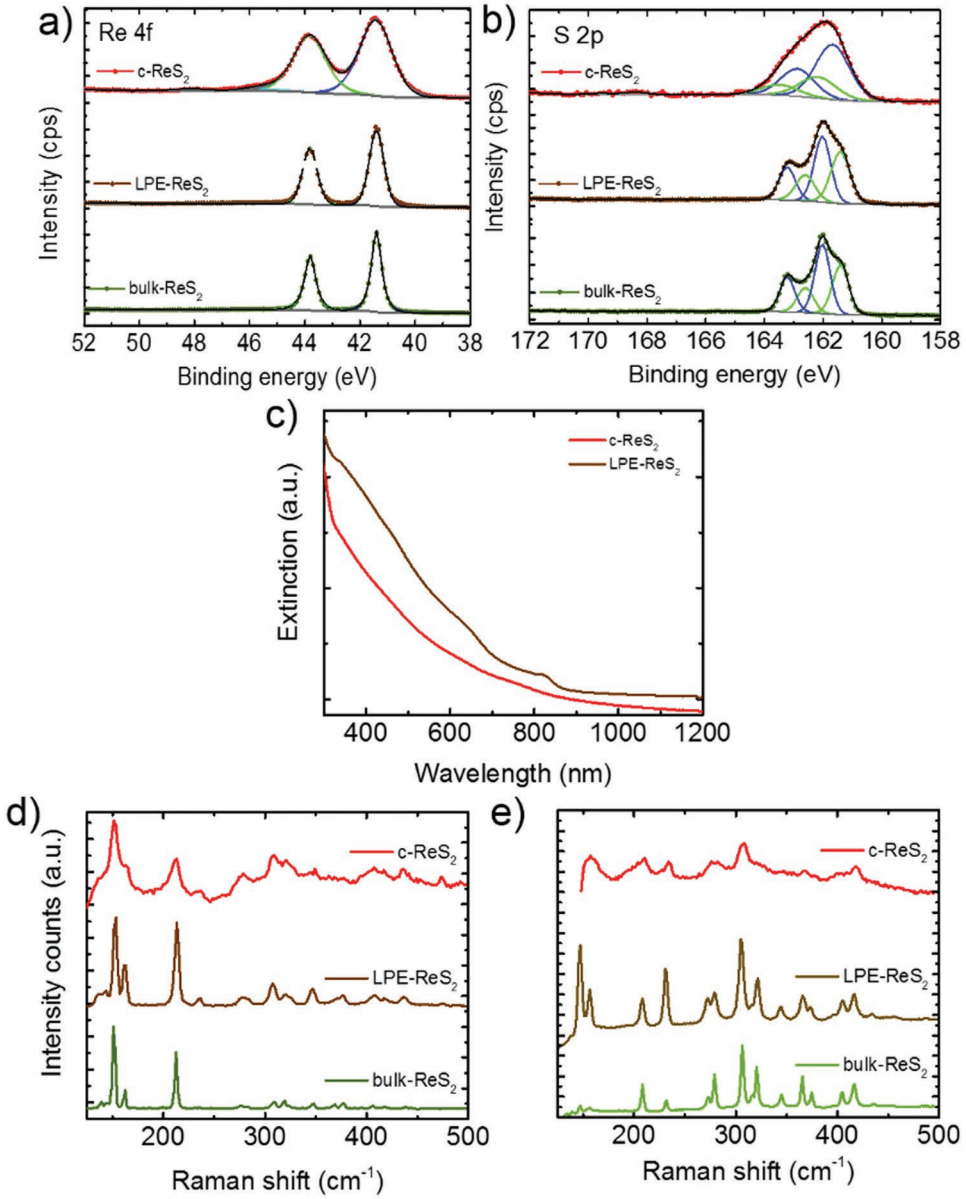

Figure 2. a,b) Re 4f and S 2p XPS core-level spectra collected from the c-ReS_2, LPE-ReS_2, and bulk-ReS_2 samples, in which the fitting reveals the deconvoluted peaks. c) Extinction spectra of c-ReS_2 and LPE-ReS_2 dispersed in toluene and isopropanol, respectively. An offset was applied to the curves for clarity. d,e) Representative Raman spectra collected at d) 532 and e) 785 nm excitation wavelength on the c-ReS_2, LPE-ReS_2, and bulk ReS_2 samples on silicon wafers.

However, we cannot discard that the two S components come from the existence of different Re—S bond lengths in the distorted ReS_2 structure, as illustrated in Scheme 1d.[12,13] For colloidal ReS_2, a good fitting of the S 2p profile was obtained by using two doublets as for the LPE and bulk-counterparts, with S $2p_{3/2}$ components at ≈161.6 and ≈162.2 eV. Moreover, XPS peaks in c-ReS_2 are broader than the ones for the LPE and bulk materials likely indicating a less crystalline structure in the colloidal case.[76] To support this statement, we also evaluated the extinction coefficient and Raman spectra of the materials, which are plotted in Figure 2c,d,e. As expected for ReS_2,[9,10,77] the c-ReS_2 material shows a strong and broad extinction from 300 to almost 1000 nm. However, in contrast to its LPE equivalent, there is no clear excitonic peak at ≈810 nm that corresponds to the E_g of the ReS_2.[77] The E_g was obtained from the $(\alpha h\nu)^n$ versus $h\nu$ (Tauc plot) analysis (see Figures S1d and S2c in the Supporting Information) using the Tauc relation $Ah\nu = Y(h\nu\text{-}E_g)^n$, in which A is the absorbance, h is Planck's constant, ν is the photon's frequency, and Y is a proportionality constant.[78] The value of the exponent denotes whether it is a direct transition ($n = 2$) or an indirect one ($n = 0.5$).[79] Since ReS_2 is a direct bandgap semiconductor, we applied $n = 2$, resulting in an E_g of ≈1.41 eV (colloidal) and ≈1.43 eV (LPE). Both values are in agreement with the theoretical (1.41 eV)[80] and experimental values (1.4–1.5 eV) from bulk to monolayer (0.7 nm) thicknesses.[15] The analysis of the Raman spectra in Figure 2d,e

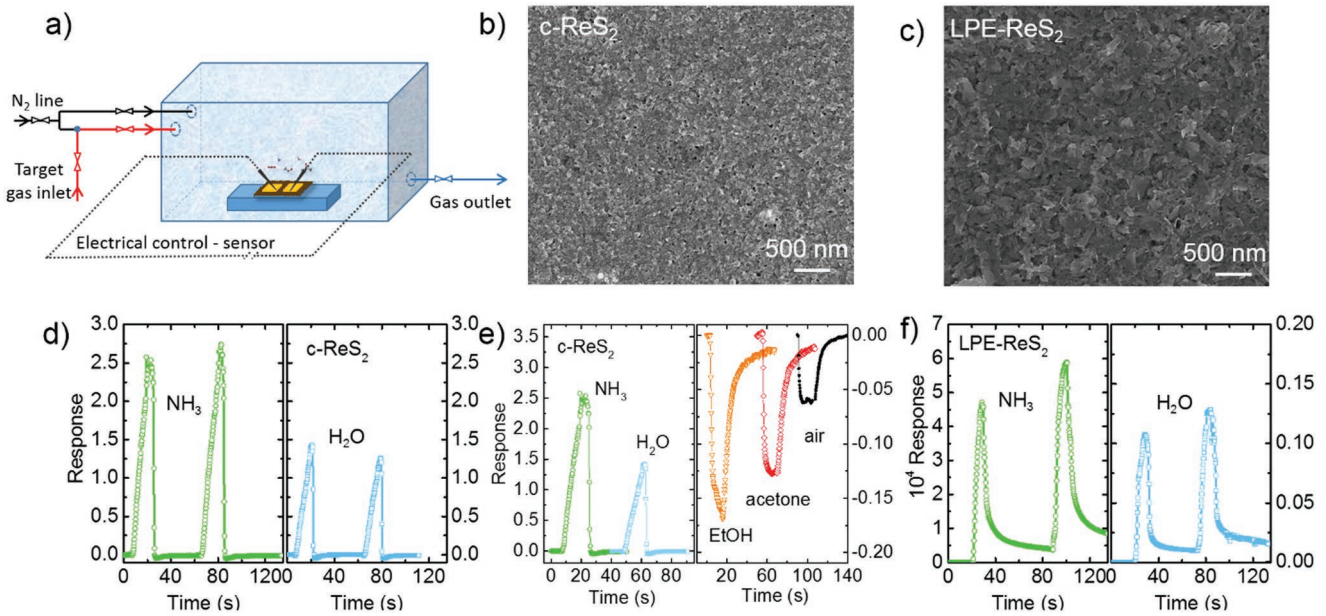

Figure 3. a) Sketch showing the chamber used for the gas sensing experiments. b,c) Representative SEM images of the colloidal and LPE-ReS_2-based gas sensors, respectively. The films (≈400 nm thickness) were prepared by drop casting the corresponding dispersions on glass substrates. d) Representative gas-induced time response of the device built with ann-ReS_2 in two consecutive cycles exposed to NH_3 (left) and H_2O (right). e) Representative gas-induced time response of the device built with ann-ReS_2 exposed to different gases: NH_3, H_2O (left), EtOH, acetone, and dry air (right). f) Representative gas-induced time response of the device built with LPE-ReS_2 exposed in two consecutive cycles to NH_3 (left) and H_2O (right). In all the cases, the gas-induced response was determined from the film conductance variation as detailed in the text.

has been performed following the detailed reports on ReS_2 carried out by Balicas' and Terrones' groups,[81,82] which identified 18 first-order modes in the 100–450 cm^{-1} range (for Raman peaks interpretation, see the Supporting Information). Since in the randomly oriented assembly of the nanosheets we cannot control the crystal orientation, we performed a comparative Raman analysis at two different excitation wavelengths, i.e., 532 and 785 nm. Independently of the excitation wavelength and synthesis batch, the Raman peaks from the colloidal sample are broader than the corresponding ones in the LPE sample. Such broader linewidth in the Raman signal of the colloidal sample indicates a lower degree of crystallinity compared to the LPE one,[83] which can be related to the difference in the temperature that is needed for their preparation. Highly crystalline ReS_2 fabricated by CVD requires a temperature >600 °C,[35] while the colloidal synthesis is performed at 350 °C. The low crystallinity of the c-ReS_2 might also be the cause for the absence of the excitonic peak in its extinction spectrum in Figure 2c.

For both colloidal and LPE samples, the following Raman modes are enhanced at 785 nm excitation compared to the 532 nm excitation, A_g^9 (273 cm^{-1}), A_g^{10} (279 cm^{-1}), A_g^{12} (305 cm^{-1}), $A_g^{13,14}$ (322 cm^{-1}), A_g^{16} (366 cm^{-1}), A_g^{17} (373 cm^{-1}), A_g^{18} (405 cm^{-1}), and A_g^3 (417 cm^{-1}), while the A_g^{15} (350 cm^{-1}) and A_g^2 (440 cm^{-1}) modes disappear, indicating that the samples are composed by few-layer (2L–4L) ReS_2 sheets, in agreement with the data reported by Terrones' group.[82] In order to prove that our colloidal synthetic approach can be versatile also for other materials, we fabricated $ReSe_2$ using Se powder as chalcogen source (see Figure S4 in the Supporting Information for synthesis details and material characterization).

In order to test the suitability of the ReS_2 sheets as films for gas sensing, and to compare the performance of the colloidal and LPE samples, we prepared their corresponding films on glass substrates by drop casting (**Figure 3**a). For the c-ReS_2 nanosheets, we used the original dispersion for drop casting, followed by annealing at 300 °C in a glovebox (3 h) to remove the organic ligands from synthesis (oleic acid and oleylamine) with the aim to make the film electrically conductive. Films from LPE samples were fabricated by drop casting without any further treatment. In this way, we obtained continuous and compact films with thickness of ≈400 nm, as shown in the scanning electron microscopy (SEM) images in Figure 3b,c (see the Experimental Section for fabrication details). The devices were completed by the evaporation of Au electrodes as contacts. All devices manifest an ohmic behavior (see Figure S5a in the Supporting Information for conductance measurements under inert –N_2– atmosphere), however the resistance of the devices made from the c-ReS_2 is much lower (460 MΩ) than the one of devices fabricated with LPE-ReS_2 (5.9 GΩ). For gas sensing via the detection of conductance changes of the film, we positioned the samples inside a chamber with controlled atmosphere connected to a probe station (see Figure 3a and the Experimental Section for details on the gas filling of the chamber and measurement protocols). From the gas flow rates we estimate the filling and purging time of the chamber to be around 1s, which is shorter than the response times that we measured on our devices. We tested the response to humidity, to NH_3 that is a toxic agent, and to ethanol (EtOH) and acetone as representative volatile organic compounds. Figure 3d–f shows the representative response ($\mathbb{R}$) for different gases of the devices obtained via the relative changes of the film conductance

(G)[51] in the presence of the target gas compared to inert (N_2) atmosphere, $\mathbb{R} = (G_{gas} - G_{inert})/G_{inert}$. The numerical values are reported in Table S1 in the Supporting Information, in which also the response in terms of resistance is given for comparison with literature.

For NH_3 and H_2O, the response of the gas sensors is positive, i.e., the conductance under the target gas is higher compared to that under the inert N_2 atmosphere. This can be explained by physisorption of the gas molecules that act as electron donors.[22,23,51,84,85] The higher response for gas sensors based on ReS_2 under NH_3 compared to air and O_2 was also reported in theoretical studies.[22] For NH_3 detection, the relative response of the devices built from LPE-ReS_2 flakes (hereafter, "LPE devices") (Figure 3f) is much higher compared to the ones fabricated from annealed c-ReS_2 (in the following noted as "colloidal devices"). However, this result is mainly related to the very low electrical conductivity of the LPE device under inert atmosphere. In fact, the recovery time of the LPE devices to the initial currents (i.e., in the nA range) is of the order of hours, while the recovery time of the colloidal devices is of the order of seconds (see Table S2 in the Supporting Information for rise and fall times of conductance response of the different devices; and Tables S3 and S4 in the Supporting Information for estimated minimum amounts detectable with the technique). In practical terms, this means that, for detection with response times of few seconds, the baseline of the LPE device is at a value of ≈1000, and therefore the relative response to NH_3 at such time scales is ≈10, while that of the colloidal device is ≈2.5–3. Concerning humidity detection, the response of the devices made from c-ReS_2 ($\mathbb{R}$ = 1.2; rise time (τ_R = 8.7 s); fall time (τ_F = 0.3 s)) outperforms clearly the ones based on LPE flakes ($\mathbb{R}$ = 8.8; τ_R = 5.2 s; τ_F = 31 s). In fact, the recovery time to return to 10% of the response after the gas flow stopped is one order of magnitude shorter for c-ReS_2 compared to the LPE flakes one. For EtOH, acetone and compressed air the conductance of the devices made from c-ReS_2 decreases compared to one achieved in inert N_2 atmosphere (Figure 3e). This result can be rationalized by oxidation of the film due to the incorporation of electron acceptor molecules.[51,84,85] Furthermore, the relative conductivity change of the devices made from c-ReS_2 exposed to EtOH, acetone and compressed air is much weaker ($\mathbb{R}_{EtOH}$ = –0.15; $\mathbb{R}_{acetone}$ = –0.12; and $\mathbb{R}_{air}$ = –0.06) and slower in recovery (EtOH: τ_R = 5.2 s; τ_F = 25 s; acetone: τ_R = 1 s; τ_F = 56 s; and air τ_R = 2.3 s; τ_F = 12 s) as compared to their exposure to NH_3 ($\mathbb{R}$ = 2.4; τ_R = 9.3 s; τ_F = 1.3 s) or H_2O ($\mathbb{R}$ = 1.2; τ_R = 8.7 s; τ_F = 0.3 s).

The circumstance that the c-ReS_2 are passivated by organic ligands opens the possibility to manipulate the film conductivity by ligand exchange with other molecules. We therefore use this approach to improve the performance of the c-ReS_2 based sensors, in terms of recovery time and response. In particular, we performed a ligand exchange process that replaces the long-chain organic ligands used in the synthesis (oleic acid and oleylamine, both with a C_{18} aliphatic chain) with shorter molecules that contain C_x aliphatic chains with $x < 4$ or an aromatic ring (see the Experimental Section for more details). Shorter ligands lead typically to stronger coupling of the nanomaterial in a compact film, which increases the charge carrier mobility.[86,87] Moreover, chemical modification of the nanomaterial surface by ligand exchange can modify the electronic properties of the material, as well as its reactivity with the functional groups of the gas molecules.[51,84] We tested different short chain molecules in this respect: 3-mercaptopropionic acid (MPA), 1,4-benzenedithiol (BDT) and 4-aminobenzoic acid (ABA), and performed the ligand exchange in solution. The films from the ligand-exchanged solutions were prepared by drop-casting, which ensured a compact film with a thickness of ≈400 nm (**Figure 4**a,b, also see Figure S6 in the Supporting Information for additional characterization). A larger S contribution in the XPS signal (compared to the samples before ligand exchange) that results from the thiol groups of the exchanged molecules confirmed the presence of MPA and BDT molecules. Concerning the exchange with ABA, the success of the ligand exchange process can only be assessed from the increase of the conductivity, since the characteristic N 1s XPS peak (NH_2, at 400.5 eV) also originates from oleylamine. The ligand-exchanged films also show ohmic conductivity, and their resistance strongly depends on the individual ligands (see Figure S5b in the Supporting Information for conductance measurements under inert –N_2– atmosphere). Here, devices made from MPA-exchanged c-ReS_2 manifested the highest conductance (R = 120 MΩ), followed by ABA (R = 510 MΩ) and BDT (R = 200 MΩ). Compared to the original device discussed in Figure 3, we achieved an increase in electrical conductivity by a factor of 4 with the MPA ligands. We tested the ligand-exchanged films for gas sensing with the same procedure as described before. Overall, we observe similar behavior before and after the ligand exchange process, with an electrical current increase under NH_3, H_2O, and CO_2, and, instead, decrease under EtOH, acetone and air. Figure 4c depicts the response of the device built from MPA-exchanged c-ReS_2 nanosheets to different gases: NH_3, H_2O, and CO_2 that lead to current increase, and EtOH, acetone and air that result in a small current decrease. Therefore, we can assume that in all the cases, colloidal, LPE, and ligand exchange fabricated devices, the sensing mechanism is based on a charge transfer between the physisorbed gas molecules and the ReS_2 structure.[51,85] Figure 4d shows the response of the gas sensors made with ligand-exchanged c-ReS_2 films when exposed to NH_3. In this context, the device made from MPA-exchanged c-ReS_2 shows the highest response ($\mathbb{R}$ = 31, with a response time of 3.3 s), followed by the ones built from BDT- and ABA-exchanged c-ReS_2. The functionalization of c-ReS_2 with BDT yields a higher sensitivity ($\mathbb{R}$ = 24 response for NH_3 detection) than ABA ($\mathbb{R}$ = 16 response for NH_3 detection), although the conductance of ABA (R_{ABA} = 510 MΩ vs R_{BDT} = 200 MΩ) is higher under inert atmosphere. The different results in terms of sensitivity and responsivity obtained without and with the functionalization of c-ReS_2, and even more, by varying the molecules used for the functionalization, point to the importance of: i) possible sites for the binding of gas molecules; ii) the efficiency of charge transfer for the gas sensing sensitivity, and iii) a good film conductivity, which is beneficial for a fast response and recovery. Here, we can expect a trade-off between a film with high surface area that is beneficial for interaction with the gas molecules, and a compact film that results in high conductivity and from which a fast response can be expected. In particular, the high sensitivity

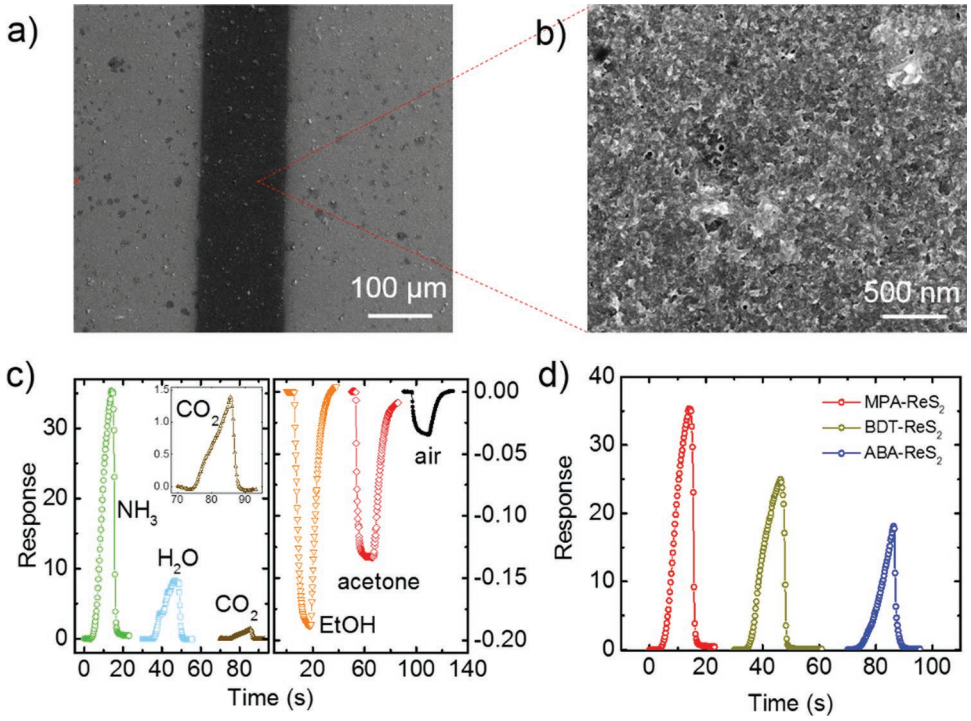

Figure 4. a,b) Representative SEM images of the device built from MPA-exchanged c-ReS_2. The film (with ≈ 400 nm thickness) was prepared by drop casting the corresponding dispersion. c) Representative gas-induced response time of the device made from MPA-exchanged c-ReS_2 under the exposure to different gases: (left) NH_3, H_2O, and CO_2, (right) EtOH, acetone, and dry air. The inset in the left panel shows the CO_2 data on a magnified scale. d) Comparison of the device performance in terms of response to NH_3 exposure for the different ligand molecules used: MPA, ABA, and BDT. In all the cases, the gas-induced response was determined from the film conductance variation as detailed in the text.

obtained with the BDT and MPA ligand exchange for NH_3 ($\mathbb{R}_{BDT}$ = 24 and $\mathbb{R}_{MPA}$ = 31, respectively) and H_2O ($\mathbb{R}_{BDT}$ = 2.4 and $\mathbb{R}_{MPA}$ = 4.5, respectively) points to a beneficial role of the SH groups of MPA and BDT for physisorption of the gas molecules and the electron transfer towards the ReS_2 film. We note that the performance of the device made from MPA-exchanged c-ReS_2 is superior to the one built with LPE-ReS_2 in Figure 3 in terms of sensitivity and response time (e.g., for NH_3 detection, $\mathbb{R}$ = 9.9, with a response time of 5.2 s for LPE-ReS_2 and $\mathbb{R}$ = 31, with a response time of 3.3 s for MPA-exchanged c-ReS_2).

The gas sensor built from MPA-exchanged c-ReS_2 outperforms, to the best of our knowledge, those reported in literature fabricated with CVD-grown ReS_2.[23] The humidity sensor reported by Yang et al.[23] made by CVD-grown ReS_2 has a resistance variation of ≈–60% at a relative humidity of 70%, with a response time of the order of tens of seconds, while our gas sensor fabricated with MPA-exchanged c-ReS_2 reaches a variation of 80% with much faster response time (4.1 s) and comparable recovery time (1 s). Gas sensing (NH_3, O_2, air) has been also reported from phototransistors made from micro-mechanically exfoliated ReS_2 flakes,[22] with a response time in the order of ms. However, this response time is related to the illumination of the device and therefore does not directly compare to our devices that work in dark condition. Concerning the gas sensors for NH_3 and EtOH based on other 2D materials, we note that our MPA-functionalized c-ReS_2 based sensor has a faster response time and better recovery of the initial conductance state than devices that use micro-mechanically exfoliated or CVD-grown MoS_2.[88,89]

Finally, we tested c-ReS_2 films as an electrocatalytic film for HER (**Figure 5**a). To make the c-ReS_2 more electrochemically active, we isolated the nanosheets from the dispersion by centrifugation and solvent evaporation. The obtained powder was then treated by thermal annealing (Ar flow, 500 °C) to remove the organic ligands from synthesis, and thereby expose the catalytically active surface of the nanosheets. After the annealing, the c-ReS_2 powder was dispersed in *N*-methyl-2-pyrrolidone (NMP) by ultrasonication, and the obtained dispersion was used for the deposition on glassy carbon (GC) rigid electrodes and single-walled carbon nanotubes (SWCNTs)-based flexible papers (i.e., buckypapers) (Figure 5b) (see the Experimental Section for more details). The choice of the SWCNT-based paper as support relies on our recent works,[61,63] in which we demonstrated a long-range (≥1 µm) electrochemical coupling between HER-active TMDCs and SWCNTs for increasing the HER-activity of TMDCs.[61,63] Moreover, the porosity of such substrate promotes the adhesion of the TMDC films without the need of ion conducting catalyst binders[61,63,90,91] (e.g., Nafion in acid solution[92] and Tokuyama AS-4 in the alkaline one[93]), which can degrade the electrocatalytic activity of the catalyst.[94,95] The GC-based electrodes were obtained by drop casting the c-ReS_2 dispersions at a mass loading of 0.13 mg cm^{-2}. The hybrid SWCNTs/c-ReS_2 electrodes were produced through a sequential vacuum filtration deposition of the material dispersions onto nylon membranes (material mass loading

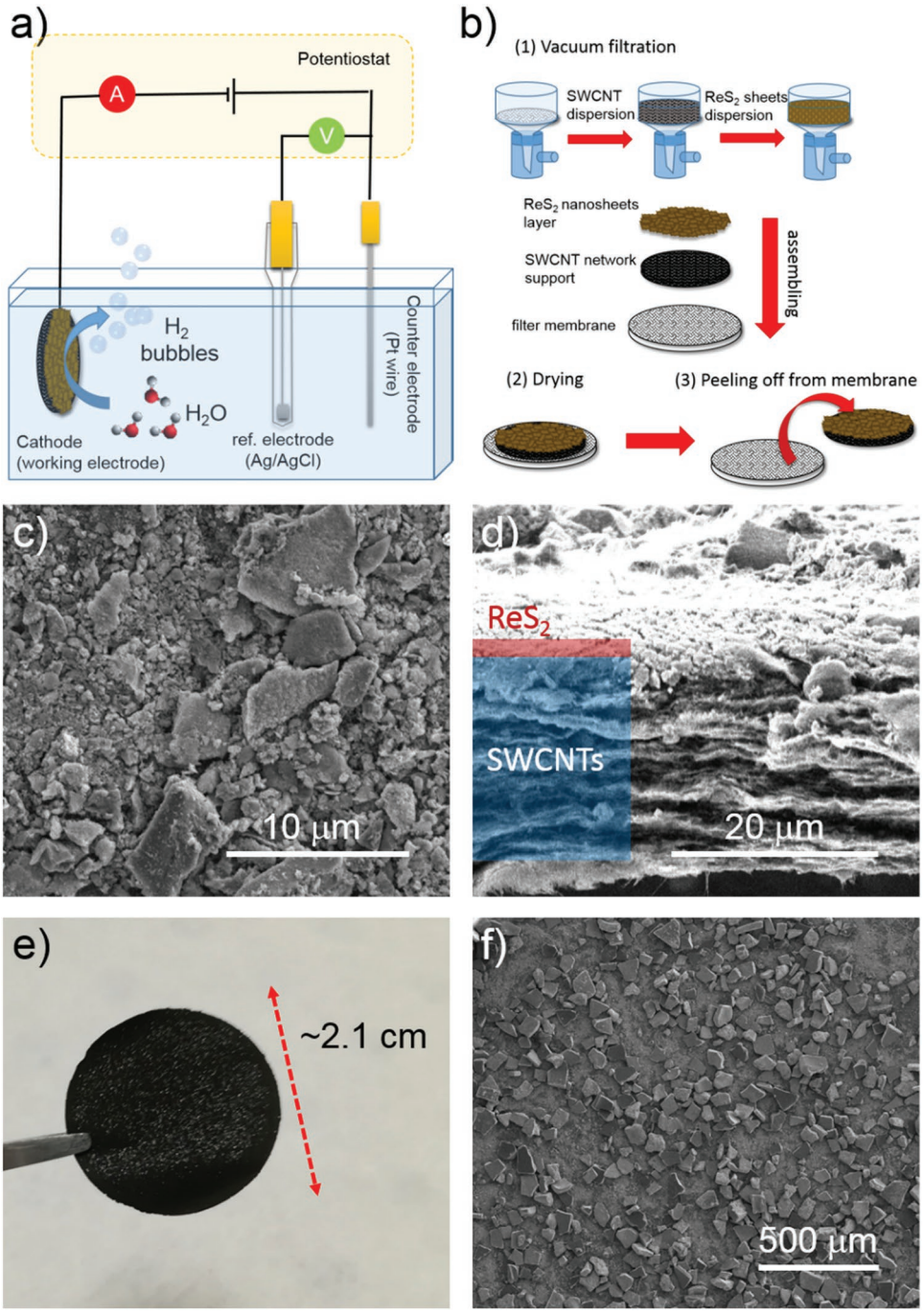

Figure 5. a) Scheme of the electrochemical setup for measuring the electrocatalysts. b) Sketch of the fabrication of the c-ReS_2-based electrodes on SWCNTs c,d) Top-view and cross-sectional SEM images of SWCNTs/c-ReS_2. e) Top-view photograph of SWCNTs/c-ReS_2 (electrode area: 3.5 cm^2). f) Top-view SEM image of SWCNTs/c-ReS_2 at higher magnification compared to the one shown in panel (c) (scale bar: 500 μm).

of 1.5 mg cm^{-2} for both SWCNTs and c-ReS_2 (5 mg of each material)). Figure 5c,d display top-view and cross-sectional SEM images of a representative SWCNTs/c-ReS_2 electrode. The c-ReS_2 form a film atop the SWCNTs network, and the electrode shows a bilayer architecture with ≈20 μm thick SWCNT-based collector and a thin c-ReS_2-based active film (thickness in the order of 1 μm). The high-magnification SEM image (Figure 5c) reveals the presence of lateral c-ReS_2 aggregates with various dimensions, in the 0.5–10 μm range. The smallest c-ReS_2 aggregates (lateral size <500 nm) penetrate the mesoporous SWCNT network (see Figure S9 in the Supporting Information). For such configuration, SWCNTs increase the electron accessibility to the HER-active sites of c-ReS_2, speeding up the HER-kinetics compared to flat GC.[61,90,96,97] Figure 5e shows a top-view photograph of the as-produced SWCNTs/c-ReS_2 (electrode area of ≈3.5 cm^2), in which the presence of

ReS_2 aggregates is visible. Such aggregates are also evident in SEM images (Figure 5f) with a lateral size ranging from 50 to 200 µm.

The HER-activity of the SWCNTs/c-ReS_2 was tested in both in acidic (0.5 M H_2SO_4) and alkaline (1 M KOH) media. In principle, the HER in acidic solution proceeds with an initial discharge of the hydronium ion (H_3O^+) and the formation of atomic H adsorbed on the electrocatalyst surface (H_{ads}), in the so-called Volmer step ($H_3O^+ + e^- \rightleftarrows H_{ads} + H_2O$), followed by either an electrochemical Heyrovsky step ($H_{ads} + H_3O^+ + e^- \rightleftarrows H_2 + H_2O$) or a chemical Tafel recombination step ($2H_{ads} \rightleftarrows H_2$). In alkaline media, the H_{ads} is formed by discharging H_2O ($H_2O + e^- \rightleftarrows H_{ads} + OH^-$). Then, either a Heyrovsky step ($H_2O + H_{ads} + e^- \rightleftarrows H_2 + OH^-$) or a chemical Tafel recombination step ($2H_{ads} \rightleftarrows H_2$) occurs. Apart from the cathodic current density η_{10}, the Tafel slope is also an important figure of merit to assess the HER-activity of an electrode.[98] However, a rigorous kinetic analysis of the HER through the Tafel slope analysis was not carried out for our electrodes, since SWCNTs hold a high surface area that leads to a remarkable capacitive current density (in the order of 1 mA cm^{-2}) even at a low LSV sweep voltage rate (≤5 mV s^{-1}). This can be the cause of misleading interpretations of the estimated kinetic parameters.[63,99]

Figure 6a,b shows the current-resistance (*iR*)-corrected polarization curves of GC/c-ReS_2 and SWCNTs/c-ReS_2 electrodes in acidic (0.5 M H_2SO_4) and alkaline (1 M KOH) aqueous solutions, respectively. The series resistance that arises from the electrical resistance of the working electrode and the electrolyte resistance, i.e., *R*, was extrapolated by single frequency electrochemical impedance spectroscopy (EIS) (see the Experimental Section for further details). The curves measured for the substrates, i.e., GC and SWCNTs, are also shown as references. The curve measured for commercial platinum on carbon (Pt/C) is reported as benchmark for HER. The c-ReS_2-based electrodes show an enhanced HER-activity compared to those of the substrates, i.e., GC and SWCNTs. Noteworthy, the use of SWCNTs as the substrate significantly increases the cathodic current densities, i.e., the HER-activity, compared to those shown by CG/c-ReS_2. Thus, in acidic media, η_{10} decreases from 0.465 V for the GC/c-ReS_2 to 0.196 V for SWCNTs/c-ReS_2. In alkaline solutions, GC/c-ReS_2 electrode is poorly HER-active (η_{10} > 0.7 V). Interestingly, SWCNTs/c-ReS_2 electrode exhibits a η_{10} of 0.299 V, indicating that the SWCNTs and c-ReS_2 interact to synergistically enhance the HER-activity of the electrode. This effect is attributed to the activity of the SWCNTs for initiating the H_2O discharge, thus accelerating the Volmer reaction on the c-ReS_2 in alkaline conditions.[100] In addition, it is worth noticing that SWCNTs/c-ReS_2 displays an HER-activity in acidic media comparable to the one shown by SWCNTs/LPE-ReS_2 (η_{10} = 0.192 V), which, however, shows a better HER-activity in alkaline media (η_{10} = 0.238 V). The morphological and electrochemical characterization of SWCNTs/LPE-ReS_2 electrode is reported in Figure S10 in the Supporting Information. Electrochemical impedance spectroscopy measurements do not show any

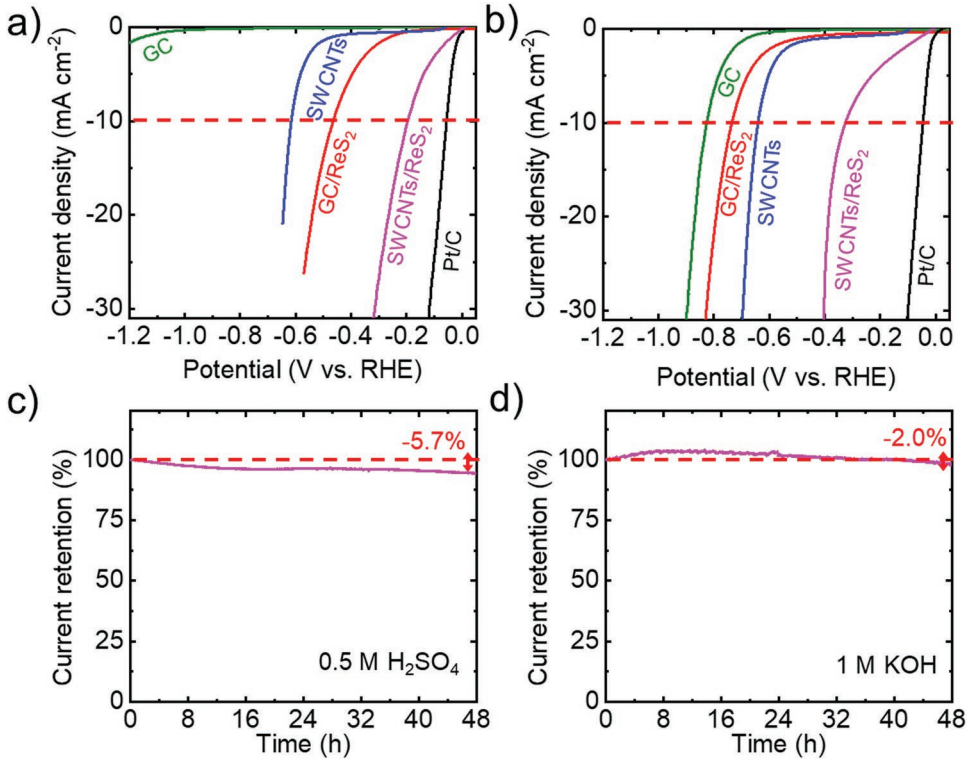

Figure 6. a,b) *iR*-corrected polarization curves measured for GC, SWCNTs, CG/c-ReS_2, SWCNTs/c-ReS_2, and Pt/C in acidic (0.5 M H_2SO_4) and alkaline (1 M KOH) solutions, respectively. c,d) Chronoamperometry measurements (current retention vs time) for the SWCNTs/c-ReS_2 electrode in 0.5 M H_2SO_4 and 1 M KOH solutions. A constant overpotential has been applied in order to give an equal starting cathodic current density of 20 mA cm^{-2}. The inset panels of (c,d) show the iR-corrected polarization curves after stability tests.

significant differences between SWCNTs/c-ReS_2 and SWCNTs/LPE-ReS_2 (see Nyquist plot in Figure S11 in the Supporting Information). Moreover, we estimated the double-layer capacitances (C_{dl}) of c-ReS_2 and LPE-ReS_2 films deposited on GC from cyclic voltammetry (CV) measurements (see for further details, Figure S12a in the Supporting Information). The calculated C_{dl} values, ≈0.162 mF cm^{-2} for c-ReS_2 film and ≈0.110 mF cm^{-2} for LPE-ReS_2 film, indicate that the electrochemical accessible surface area of c-ReS_2 film is superior to the one of the LPE-ReS_2 film. The larger accessible surface area of c-ReS_2 (≈ 4 ± 1 nm determined by TEM), compared to the LPE-ReS_2, can be attributed to the small lateral size of the c-ReS_2, as well as their arrangement relatively to the substrate (see Figure S12b,c in the Supporting Information).

Beyond the electrocatalytic activity, the durability is another important criterion for the exploitation of an electrocatalyst. Figure 6c,d shows the chronoamperometry measurements (current retention vs time) for SWCNTs/c-ReS_2, in acidic and alkaline solutions, respectively. A constant overpotential was applied in order to provide the same starting cathodic current density of 20 mA cm^{-2} for HER. Glassy carbon rod has been used as counter-electrode to avoid Pt dissolution/re-deposition effects altering the HER-activity of working electrode in presence of Pt-based counter electrodes. In both acidic and alkaline media, SWCNTs/c-ReS_2 exhibit a nearly stable behavior over 48 h (current retention of 94.3% and 98.0%, respectively). The slight fluctuation of the HER-activity can be tentatively attributed to morphological changes of the electrode film during the HER process. Similar effects have been previously observed in electrocatalysts based on metallic TMDCs, such as TaS_2[101] and NbS_2[91,102] nanosheets, as well as in other 2D material-based electrodes, including graphene-based electrocatalysts.[103] In fact, the mechanical stresses originated by H_2 bubbling can cause a re-orientation/fragmentation of the 2D electrocatalysts, which, consequently, shows higher electrochemically accessible surface area.[101,102,104] Moreover, such mechanical stresses occasionally caused the formation of cracks in the active material films, as observed by SEM image analysis of additional electrodes (Figure S13, Supporting Information). This led to a significant change of the cathodic current of the electrodes over time in both acidic and alkaline media. For example, in acidic media some electrodes reported an increase of the initial HER-activity over 24 h, achieving a η_0 = 0.162 V versus RHE (see Figure S14a in the Supporting Information). This behavior might be attributed to the progressive increase of the H^+ accessibility to the HER-active sites of the electrodes.[101,102,104] In alkaline media, the electrodes often displayed an increase of the electrical resistance (e.g., from 4.4 to 45.9 Ω, measured by single frequency EIS), which caused a decrease of 21.5% of the initial current density (see Figure S14b, Supporting Information). Despite the decrease of the HER-activity of the electrode, the *iR*-corrected polarization curves shows an electrochemical activation of the c-ReS_2 after 24 h (η_{10} reduced from 0.327 to 0.181 V), similarly to the electrodes tested in acidic media. The use of electrocatalyst binders, such as sulfonated tetrafluoroethylene-based fluoropolymer copolymers (e.g., Nafion), could prospectively "freeze" an optimized electrode morphology of the current electrodes, as well as an increase of the electrode durability under HER-operation.

Table 1 summarizes the η_{10} achieved by our electrode in comparison with those reported by different literature results on ReS_2-based electrocatalysts, as well as other promising electrocatalysts based on other TMDCs (MoS_2,[67,96,105–107] WS_2,[108] and $MoSe_2$[61]) and phosphides ($NiCo_2P_x$).[109] In particular, in acidic solution, η_{10} of SWCNTs/ReS_2 (0.196, 0.162 V after 24 h stability test) approaches the best values obtained by ReS_2-based electrocatalysts (0.147 V),[54] which come from a defect-activated monolayer ReS_2 grown by CVD. These results indicate that there is still room for improvement in our system by properly optimizing the material surface in future experiments, as it has also been demonstrated for other TMDCs.[105,110,111] Additionally, the HER-performance of our electrocatalysts are comparable or superior to those previously reported for electrocatalysts based on other TMDCs (η_{10} values between 0.170 and 0.372 V), concretely, in absence of either mechanical strain or doping effects, including the most studied MoS_2,[67,96,105–107] WS_2,[108] and $MoSe_2$.[61] The relevant electrocatalytic properties of ReS_2 have been recently attributed to the presence of metal—metal bonds (not present for group-VI_B TMDCs),[9,11–13] which are highly HER-active sites in presence of vacancies causing an intrinsic HER-promoting optimization of the electronic charge distribution.[54] Moreover, we reported here also the HER-activity of ReS_2-based electrocatalyst in alkaline conditions, providing new insight for the development of pH-universal electrocatalysts to be exploited as cathode materials in current large-scale H_2 production technologies,[112–114] e.g., chloro-alkaline systems[115] or alkaline zero-gap water electrolysis units,[116] and proton exchange membrane (PEM) electrolysis.[117,118]

3. Conclusions

We report a bottom-up approach for the synthesis of colloidal ReS_2 (c-ReS_2) nanosheets that relies on low fabrication temperatures (below 360 °C) and process times inferior to 4 h. We use elemental sulfur as source, which is more accessible and environmentally friendly than other precursor materials currently used in the colloidal synthesis of different TMDCs. Drop-cast c-ReS_2-based films are tested as gas sensors for a variety of agents, achieving highly competitive performance after annealing or ligand exchange in comparison with devices built with CVD-ReS_2 or -MoS_2. Furthermore, the colloidal ReS_2 nanosheets were tested as HER-electrocatalysts operating both in alkaline and acidic media. In particular, electrodes made by c-ReS_2 films deposited on SWCNT (SWCNTs/c-ReS_2) exhibit overpotentials at a cathodic current density of 10 mA cm^{-2} (η_{10}) of 0.196 V in 0.5 M in H_2SO_4 and 0.299 V in 1 M KOH. In acidic media, the η_{10} of SWCNTs/c-ReS_2 approaches the best values obtained by CVD-grown defect-activated ReS_2-based electrocatalysts. In comparison with nonoptimized electrocatalysts based on other group-VI_B TMDCs, the ReS_2-based electrocatalysts here developed exhibit similar or even superior HER-activity. The c-ReS_2 can therefore present a promising solution for the fabrication of gas sensors and HER electrocatalysts, with still considerable room for improvement by exploiting device designs and finely tuned surface modifications.

Table 1. Summary of the η_{10} values measured for our electrodes and other ReS_2-based electrocatalysts reported in literature in acid and basic conditions. For comparison we also show η_{10} values measured for electrocatalysts based on MoS_2, $MoSe_2$, WS_2, and phosphides.

Electrocatalyst	η_{10} [V]	Electrolyte	Mass loading [mg cm^{-2}]	Ref.
GC/ReS_2	0.465	0.5 M H_2SO_4	≈0.13	This work
	0.735	1 M KOH		
SWCNTs/ReS_2	0.195 (0.162 after 24 h)	0.5 M H_2SO_4	≈1.59	This work
	0.327 (0.181 after 24 h)	1 M KOH		
Chemically exfoliated ReS_2 nanosheets	≈0.3[a)]	0.5 M H_2SO_4	Not reported	[36]
Defects-activated monolayer ReS_2	0.147	0.5 M H_2SO_4	Monolayer	[54]
Vertically Oriented Arrays of ReS_2 Nanosheets	≈0.3	0.5 M H_2SO_4	≈0.67	[25]
Lithiated Vertically Oriented Arrays of ReS_2 Nanosheets	≈0.2	0.5 M H_2SO_4	≈0.67 (excluding Li)	[25]
ReS_2 3D reticulated vitreous carbon foams	0.336[a)]	0.5 M H_2SO_4	Not reported (ReS_2 grown onto carbon foam)	[28]
One-pot synthetized ReS_2	>0.35	0.5 M H_2SO_4	0.02	[119]
MoS_2	> 0.35	0.5 M H_2SO_4	Monolayer	[105]
MoS_2 with S vacancies	0.25	0.5 M H_2SO_4		
Strained MoS_2 with S vacancies	0.17	0.5 M H_2SO_4		
Co-doped MoS_2	0.159	0.5 M H_2SO_4	0.5	[110]
Reduced graphene oxide:MoS_2 hybrid on GC	≈0.15	0.5 M H_2SO_4	0.285	[111]
Reduced graphene oxide:MoS_2 hybrid on carbon fibers	≈0.15	0.5 M H_2SO_4	1	
MoS_2 nanosheets	> 0.3	0.5 M H_2SO_4	0.05	[67]
Metallic (1T) MoS_2 nanosheets	≈0.20	0.5 M H_2SO_4	0.05	
Liquid-phase exfoliated MoS_2	0.372	0.5 M H_2SO_4	0.5	[96]
Graphene/MoS_2	0.175	0.5 M H_2SO_4	0.5	
Chemically exfoliated metallic (1T)-MoS_2	0.235	0.5 M H_2SO_4	0.5	
CVD-grown MoS_2 monolayer on GC	0.342	0.5 M H_2SO_4	Not reported	[106]
Solvothermal produced MoS_2 on GC	0.252	0.5 M H_2SO_4	≈0.5	[107]
Liquid-phase exfoliated $MoSe_2$	0.37	0.5 M H_2SO_4	2	[61]
SWCNTs/$MoSe_2$	0.17	0.5 M H_2SO_4	2	[61]
WS_2 nanosheets	>150	0.5 M H_2SO_4	0.35	[108]
$NiCo_2P_x$ Nanowires	0.104	0.5 M H_2SO_4	5.9	[109]

[a)]Data not *iR*-corrected.

4. Experimental Section

Materials: Rhenium (V) chloride ($ReCl_5$, 99.9%, Alfa Aesar); sulfur powder (99%, Strem Chemicals); oleic acid (OA, 90%, Sigma Aldrich, degassed at 100 °C 2 h); oleylamine (OlAm, 70%, Sigma Aldrich); 1-octadecene (ODE, 90%, Sigma Aldrich, degassed at 150 °C 3 h); acetone (≥99.5%, Sigma Aldrich); ethanol (EtOH, (≥99.8, without additive, Sigma Aldrich); methanol (MeOH, ≥99.8%, Sigma Aldrich); 2-propanol (IsOH, ≥99.8%, Sigma Aldrich); 3-mercaptopropionic acid (MPA, ≥99%, Sigma Aldrich); 4-aminobenzoic acid (ABA, ≥99%, Sigma Aldrich); 1,4-benzenedithiol (BDT, 97%, Alfa Aesar). Au pellets (99.999%) were purchased from Kurt J. Lesker.

Colloidal Synthesis of ReS_2 Nanosheets: The general procedure to obtain c-ReS_2 consists in the use of two separated precursor solutions: one in the round-bottom flask and the second one added by syringe pump method. For the reaction, a metal:chalcogenide molar ratio of 1:6 was used . The dispersion that contained the Re precursor ($ReCl_5$ 67 mg) was prepared by sonication in a bath at 60 °C (1 h) with 500 µL OA + 2 mL ODE. This was added by syringe pump (rate 2 mL h^{-1}) in a hot medium under Ar flow (350 °C) of S-OlAm. The synthesis medium itself was prepared by mixing 35 mg S with 7 mL OlAm and degassing under Ar during 2 h at 250 °C in a Schlenk line until a clear orange-brownish solution was achieved. The reaction temperature was set to 350 °C. The suspension as obtained from synthesis was purified twice (in air) by adding toluene, acetone, and isopropanol (15:10:5 mL), followed by centrifugation (2599 × *g*, Sigma 3-16P centrifuge, rotor 19776). The sheets were finally dispersed in toluene using a vortex.

TEM: The morphology of the synthesized c-ReX_2 nanosheets and LPE-ReX_2 (X = S or Se) flakes was evaluated by transmission electron microscopy in a JEOL JEM-1011 microscope (W filament), operated at 100 kV. Samples were drop cast on carbon-coated copper grids. Selected area electron diffraction patterns and overview TEM images were also acquired with a JEOL JEM-1400Plus TEM, with a thermionic source (LaB_6 crystal), operated at 120 kV. Selected area electron diffraction pattern processing (azimuthal integration, background subtraction) was done using the PASAD plugin for Digital Micrograph.[120] High-angle annular dark-field scanning TEM and bright-field TEM imaging at higher magnification of the c-ReX_2 nanosheets (X = S or Se) samples were carried out by using a FEI Tecnai G^2 F20, with Schottky emitter, operated at 200 kV. Statistics for the estimation of the lateral size and thickness were carried out considering 20 individual domains in the nanosheets for each sample.

Atomic force microscopy (AFM): AFM images were acquired by using a Nanowizard III (JPK Instruments, Germany) mounted on an Axio Observer D1 (Carl Zeiss, Germany) inverted optical microscope. The samples were prepared by drop casting c-ReS_2 flakes dispersion onto a freshly cleaved mica substrate (G250-1, Agar Scientific Ltd., Essex, U.K.) and the AFM measurements were carried out by using PPP-NCHR cantilevers (Nanosensors, USA) with a nominal tip diameter of 10 nm. Intermittent contact mode AFM images of 5×5 μm^2 and 1.5×1.5 μm^2 were collected with 1024 data points per line and the working set point is kept above 70% of the free oscillation amplitude. The scan rate for the acquisition of images was 0.9 Hz. Height profiles were processed by using the JPK Data Processing software (JPK Instruments, Germany) and the data were analyzed with OriginPro 9.1 software.

XPS: X-ray photoelectron spectroscopy was carried out in a Kratos Axis UltraDLD spectrometer using a monochromatic Al K a source (15 kV, 20 mA). High-resolution scans were performed at a constant pass energy of 10 eV and steps of 0.1 eV. The photo-electrons were detected at a take-off angle $\varphi = 0°$ with respect to the surface normal. The pressure in the analysis chamber was kept below 7×10^{-9} Torr. The binding energy scale was internally referenced to the Au $4f^{7/2}$ peak at 84 eV. The spectra were analyzed using the CasaXPS software (Version 2.3.16).

Raman Spectroscopy Characterization: Raman measurements were performed in a Renishaw inVia micro-Raman microscope equipped with a 50× (0.75 N.A.) objective with excitation wavelengths of 532 and 785 nm and an incident power ≤1 mW to avoid heating and damage of the samples. The samples were prepared by drop casting the diluted materials dispersion onto a Si wafer covered with 300 nm thermally grown SiO_2 (LDB Technologies Ltd.). For each sample, at least 50 spectra were collected.

Fabrication of the Gas Sensors: A ligand exchange procedure in solution was carried out with the as-prepared OA/OlAm-capped ReS_2 nanosheets dispersed in toluene. The different ligands (MPA, ATP and BDT) were dissolved in MeOH at a concentration of 1×10^{-3} M. The c-ReS_2 dispersion in toluene (50 mg mL^{-1}) and the ligand solution were mixed in a volume ratio of 1:1 and stirred 2 min in a vortex, following by centrifugation (5000 rpm) and removal of the supernatant. Then, procedure was repeated once more, with a subsequent purification step with toluene: MeOH twice and centrifugation. Finally, the ligand exchanged ReS_2 nanosheets were dispersed in isopropanol at a concentration of 50 mg mL^{-1}, and immediately used for the preparation of the films on cleaned glass slides (≈1.5×1.5 cm^2) by drop casting (100 µL). Prior to the deposition, the glass substrates were cleaned in an ultrasonic bath (8 min each step), first with acetone, followed by isopropanol, dried with a N_2 flow, and finally cleaned under N_2 plasma (100 W, 2 min). For the Au contacts deposition, a shadow mask with square holes of 1×1 mm^2 area, separated by 100 µm, was used. The Au film with a thickness of 80 nm was evaporated in a Kenosistec e-beam evaporator at a deposition rate of 0.3 Å s^{-1} and base pressure of about 1.0 10^{-6} mbar. The thickness of the different films was measured with a Veeco Dektak 150 profilometer.

Electrical Characterization of the Gas Sensors: The electrical tests were carried out in a chamber (see Figure 3a) equipped with two inlets, one for the N_2 and the other for the target gases. Side ports allow the access of micromanipulators connected to a Keithley 2612 source-meter. The chamber (≈643 cm^3) had a transparent top lid, so that positioning of the tips was possible by eye. A N_2 line, at a pressure slightly above ambient pressure (1.2 bar, flow of ≈667 cm^3 s^{-1} determined with a flowmeter (Yokogawa)), provided the inert atmosphere used as reference and allows to fill and purge the chamber in ≈1 s. A glass bubbler was connected and used for containing the water (MilliQ), ammonia (2% vol aq. solution), EtOH and acetone while bubbling with the N_2 flow used as carrier to create the saturated atmosphere. To ensure uniform evaporation of the volatile gases, the bubbler was kept in a warm water bath (60 °C). For CO_2 and compressed dry air, reservoirs connected to the experimental chamber were used. The experiments were performed according to the following procedure: current was measured as a function of time, first under N_2 flux, then the test gas was injected in the chamber for 10 s, then the flux was switched back to N_2 until recovery of the base current. The procedure was repeated multiple times for each device to ensure reproducibility.

Fabrication of the Electrocatalyst Electrodes: The solvent was removed from the as-prepared (c-ReS_2) sample by bubbling with nitrogen. The obtained powder was annealed in a tubular furnace (PSC 12/-/600H, Lenton, UK, 25 mm inner tube diameter, Ar 100 sccm) at 500 °C for 8 h. Then, the powder was dispersed in NMP at a concentration of 1 mg mL^{-1} and sonicated for 7 h. The GC/c-ReS_2 electrodes were prepared by drop casting the c-ReS_2 NMP dispersion (0.2 mg) on GC substrates (Sigma Aldrich) with geometrical area of 1×1.5 cm^2 (c-ReS_2 mass loading ≈0.13 mg cm^{-2}). Electrodes of Pt/C were produced as benchmark for HER by depositing the Pt/C dispersion onto GC substrates. The Pt/C dispersion was produced by dissolving 4 mg of Pt/C (5 wt% Pt loading, Sigma Aldrich) and 80 µL of Nafion solution (5 wt%, Sigma Aldrich) in 1 mL of 1:4 v/v ethanol/water. The Pt/C mass loading of the electrodes was 0.262 mg cm^{-2}, in agreement with protocols developed previously.[100,103] The SWCNTs/c-ReS_2 electrodes were fabricated by sequential vacuum filtrations of 5 mg of SWCNTs (>90%, Cheap Tubes, sonic-tip de-bundled in NMP at a 0.4 mg mL^{-1} concentration[61,63]) and 5 mg of c-ReS_2 on nylon filter membranes (0.2 µm pore size, 25 mm diameter from Sigma Aldrich). The as-produced films (geometrical area = 3.5 cm^2, and c-ReS_2 mass loading ≈1.59 mg cm^{-2}) spontaneously peeled off the nylon membrane during the drying, resulting in self-standing electrodes ready to be used. The SWCNTs/LPE-ReS_2 electrodes were produced using the same protocols described for SWCNTs/c-ReS_2, except for the use of the as-produced LPE-ReS_2 dispersion in isopropanol instead of c-ReS_2 one. Additional electrodes were produced by depositing the c-ReS_2 and LPE-ReS_2 nanosheet dispersions onto GC by drop casting method (catalyst mass loading = 0.2 mg cm^{-2}). All the electrodes were dried overnight at room temperature before their electrochemical characterization.

Electrochemical Measurements of the Electrodes: Measurements were carried out at room temperature in a flat-bottom quartz cell under a three-electrode configuration using an Ivium CompactStat potentiostat/galvanostat station controlled via IviumSoft. A Pt wire or a GC rod were used as the counter electrode and a KCl-saturated Ag/AgCl was used as the reference electrode. As aqueous medium, 200 mL of two aqueous solutions were used: 0.5 M H_2SO_4 (99.999%, Sigma-Aldrich) and 1 M KOH (90%, Sigma Aldrich). MilliQ water was used to prepare the solutions. Oxygen was purged from electrolyte solutions by flowing N_2 throughout the aqueous medium using a porous frit for 30 min before starting the measurements. A constant N_2 flow was kept afterward for the whole duration of the experiments to avoid re-dissolution of O_2 in the electrolyte. The potential difference between the working electrode and the Ag/AgCl reference electrode was converted to the RHE scale using the Nernst equation: $E_{RHE} = E_{Ag/AgCl} + 0.059pH + E^0_{Ag/AgCl}$, where E_{RHE} is the converted potential versus RHE, $E_{Ag/AgCl}$ is the potential experimentally measured against the Ag/AgCl reference electrode, and $E^0_{Ag/AgCl}$ is the standard potential of Ag/AgCl at 25 °C (0.1976 V). The LSV curves were acquired at the scan rate of 5 mV s^{-1}. Polarization curves were *iR*-corrected, in which *i* is the measured working electrode current and the *R* is the series resistance that arises from the working electrode substrate and electrolyte resistances. *R* was extrapolated by the real part of the impedance (Re[Z]) measured by single frequency EIS at open-circuit potential and at the frequency of 100 kHz. Electrochemical impedance spectra of the SWCNTs/c-ReS_2 and SWCNTs/LPE-ReS_2 were acquired at open circuit potential at frequencies between 0.1 Hz and 200 kHz. Stability tests were carried out by chronoamperometry measurements (*j*–*t* curves) by measuring the current in the potentiostatic mode at a fixed overpotential in order to provide the same starting cathodic current density of 20 mA cm^{-2} for HER. The C_{dl} of the c-ReS_2 and LPE-ReS_2 films deposited onto GC were estimated by CV measurements in a non-Faradaic region of potential (i.e., potential between 0.30 and 0.45 V vs Ag/AgCl) at various potential scan rates (from 20 to 800 mV s^{-1}) in 0.5 M H_2SO_4.

SEM/EDX Characterization: SEM/EDX measurements were performed on the sensor devices and electrode samples using a Helios Nanolab

600 (FEI Company) microscope. SEM measurements were performed at 5 kV and 0.2 nA. For the cross-section images, the electrodes were carefully cut with a scalpel and measured in 90° tilted sample holder.

Supporting Information

Supporting Information is available from the Wiley Online Library or from the author.

Acknowledgements

This project received funding from the European Union's Horizon 2020 research and innovation programme under grant agreement no. 785219 (GrapheneCore2), and the European Research Council (grant agreement no. 714876 PHOCONA). The authors thank Dr. A. Toma for the access to the IIT clean room facilities for the SEM measurements and evaporation procedures, Dr. F. de Angelis for the access to the Raman lab and the Materials Characterization and Electron Microscopy facilities for the access to the XPS equipment and TEM, respectively. M. Leoncini is acknowledged for the support in the fabrication of the gas chamber.

Conflict of Interest

The authors declare no conflict of interest.

Keywords

colloidal synthesis, electrocatalysts, gas sensors, hydrogen evolution reaction, transition metal dichalcogenides

Received: August 19, 2019
Revised: November 4, 2019
Published online: December 1, 2019

[1] R. Lv, J. A. Robinson, R. E. Schaak, D. Sun, Y. Sun, T. E. Mallouk, M. Terrones, *Acc. Chem. Res.* **2015**, *48*, 56.
[2] Z. Lin, A. McCreary, N. Briggs, S. Subramanian, K. Zhang, Y. Sun, X. Li, N. J. Borys, H. Yuan, S. K. Fullerton-Shirey, A. Chernikov, H. Zhao, S. McDonnell, A. M. Lindenberg, K. Xiao, B. J. LeRoy, M. Drndić, J. C. M. Hwang, J. Park, M. Chhowalla, R. E. Schaak, A. Javey, M. C. Hersam, J. Robinson, M. Terrones, *2D Mater.* **2016**, *3*, 042001.
[3] J. H. Han, M. Kwak, Y. Kim, J. Cheon, *Chem. Rev.* **2018**, *118*, 6151.
[4] W. S. Yun, S. W. Han, S. C. Hong, I. G. Kim, J. D. Lee, *Phys. Rev. B* **2012**, *85*, 033305.
[5] P. Tonndorf, R. Schmidt, P. Böttger, X. Zhang, J. Börner, A. Liebig, M. Albrecht, C. Kloc, O. Gordan, D. R. T. Zahn, S. Michaelis de Vasconcellos, R. Bratschitsch, *Opt. Express* **2013**, *21*, 4908.
[6] X. Chia, A. Y. S. Eng, A. Ambrosi, S. M. Tan, M. Pumera, *Chem. Rev.* **2015**, *115*, 11941.
[7] X. Liu, T. Galfsky, Z. Sun, F. Xia, E. Lin, Y.-H. Lee, S. Kéna-Cohen, V. M. Menon, *Nat. Photonics* **2015**, *9*, 30.
[8] A. A. Tedstone, D. J. Lewis, P. O'Brien, *Chem. Mater.* **2016**, *28*, 1965.
[9] M. Rahman, K. Davey, S.-Z. Qiao, *Adv. Funct. Mater.* **2017**, *27*, 1606129.
[10] M. Hafeez, L. Gan, A. Saleem Bhatti, T. Zhai, *Mater. Chem. Front.* **2017**, *1*, 1917.
[11] D. A. Chenet, O. B. Aslan, P. Y. Huang, C. Fan, A. M. van der Zande, T. F. Heinz, J. C. Hone, *Nano Lett.* **2015**, *15*, 5667.
[12] H. H. Murray, S. P. Kelty, R. R. Chianelli, C. S. Day, *Inorg. Chem.* **1994**, *33*, 4418.
[13] S. P. Kelty, A. F. Ruppert, R. R. Chianelli, J. Ren, M.-H. Whangbo, *J. Am. Chem. Soc.* **1994**, *116*, 7857.
[14] K. Momma, F. Izumi, *J. Appl. Crystallogr.* **2011**, *44*, 1272.
[15] S. Tongay, H. Sahin, C. Ko, A. Luce, W. Fan, K. Liu, J. Zhou, Y.-S. Huang, C.-H. Ho, J. Yan, D. F. Ogletree, S. Aloni, J. Ji, S. Li, J. Li, F. M. Peeters, J. Wu, *Nat. Commun.* **2014**, *5*, 3252.
[16] H. Jang, C. R. Ryder, J. D. Wood, M. C. Hersam, D. G. Cahill, *Adv. Mater.* **2017**, *29*, 1700650.
[17] O. B. Aslan, D. A. Chenet, A. M. van der Zande, J. C. Hone, T. F. Heinz, *ACS Photonics* **2016**, *3*, 96.
[18] S.-H. Jo, H.-Y. Park, D.-H. Kang, J. Shim, J. Jeon, S. Choi, M. Kim, Y. Park, J. Lee, Y. J. Song, S. Lee, J.-H. Park, *Adv. Mater.* **2016**, *28*, 6711.
[19] M. Hafeez, L. Gan, H. Li, Y. Ma, T. Zhai, *Adv. Funct. Mater.* **2016**, *26*, 4551.
[20] B. Jariwala, D. Voiry, A. Jindal, B. A. Chalke, R. Bapat, A. Thamizhavel, M. Chhowalla, M. Deshmukh, A. Bhattacharya, *Chem. Mater.* **2016**, *28*, 3352.
[21] G. Nazir, M. A. Rehman, M. F. Khan, G. Dastgeer, S. Aftab, A. M. Afzal, Y. Seo, J. Eom, *ACS Appl. Mater. Interfaces* **2018**, *10*, 32501.
[22] S. Yang, J. Kang, Q. Yue, J. M. D. Coey, C. Jiang, *Adv. Mater. Interfaces* **2016**, *3*, 1500707.
[23] A. Yang, J. Gao, B. Li, J. Tan, Y. Xiang, T. Gupta, L. Li, S. Suresh, J. C. Idrobo, T.-M. Lu, M. Rong, N. Koratkar, *2D Mater.* **2016**, *3*, 045012.
[24] Q. Zhang, S. Tan, R. G. Mendes, Z. Sun, Y. Chen, X. Kong, Y. Xue, M. H. Rümmeli, X. Wu, S. Chen, L. Fu, *Adv. Mater.* **2016**, *28*, 2616.
[25] J. Gao, L. Li, J. Tan, H. Sun, B. Li, J. C. Idrobo, C. V. Singh, T.-M. Lu, N. Koratkar, *Nano Lett.* **2016**, *16*, 3780.
[26] Q. Li, Y. Xu, Z. Yao, J. Kang, X. Liu, C. Wolverton, M. C. Hersam, J. Wu, V. P. Dravid, *ACS Nano* **2018**, *12*, 7875.
[27] A.-J. Cho, S. D. Namgung, H. Kim, J.-Y. Kwon, *APL Mater.* **2017**, *5*, 076101.
[28] L. Wang, Z. Sofer, J. Luxa, D. Sedmidubský, A. Ambrosi, M. Pumera, *Electrochem. Commun.* **2016**, *63*, 39.
[29] Q. Zhang, W. Wang, J. Zhang, X. Zhu, Q. Zhang, Y. Zhang, Z. Ren, S. Song, J. Wang, Z. Ying, R. Wang, X. Qiu, T. Peng, L. Fu, *Adv. Mater.* **2018**, *30*, 1707123.
[30] Live PGM Prices, https://www.metalsdaily.com/live-prices/pgms, (accessed: March 2019).
[31] Engelhard Industrial Bullion (EIB) Prices, https://apps.catalysts.basf.com/apps/eibprices/mp/, (accessed: March 2019).
[32] K. Keyshar, Y. Gong, G. Ye, G. Brunetto, W. Zhou, D. P. Cole, K. Hackenberg, Y. He, L. Machado, M. Kabbani, A. H. C. Hart, B. Li, D. S. Galvao, A. George, R. Vajtai, C. S. Tiwary, P. M. Ajayan, *Adv. Mater.* **2015**, *27*, 4640.
[33] N. Al-Dulaimi, D. J. Lewis, X. L. Zhong, M. Azad Malik, P. O'Brien, *J. Mater. Chem. C* **2016**, *4*, 2312.
[34] Y. Kim, B. Kang, Y. Choi, J. H. Cho, C. Lee, *2D Mater.* **2017**, *4*, 025057.
[35] F. Cui, C. Wang, X. Li, G. Wang, K. Liu, Z. Yang, Q. Feng, X. Liang, Z. Zhang, S. Liu, Z. Lei, Z. Liu, H. Xu, J. Zhang, *Adv. Mater.* **2016**, *28*, 5019.
[36] T. Fujita, Y. Ito, Y. Tan, H. Yamaguchi, D. Hojo, A. Hirata, D. Voiry, M. Chhowalla, M. Chen, *Nanoscale* **2014**, *6*, 12458.
[37] N. Al-Dulaimi, E. A. Lewis, D. J. Lewis, S. K. Howell, S. J. Haigh, P. O'Brien, *Chem. Commun.* **2016**, *52*, 7878.
[38] J. Kang, V. K. Sangwan, J. D. Wood, X. Liu, I. Balla, D. Lam, M. C. Hersam, *Nano Lett.* **2016**, *16*, 7216.
[39] H. Weller, J. Niehaus, *GB2457314A*, **2009**.
[40] H. Weller, J. Niehaus, *WO2009101091A1*, **2009**.
[41] H. Weller, J. Niehaus, *US9084979B2*, **2015**.

[42] D. Son, S. I. Chae, M. Kim, M. K. Choi, J. Yang, K. Park, V. S. Kale, J. H. Koo, C. Choi, M. Lee, J. H. Kim, T. Hyeon, D.-H. Kim, *Adv. Mater.* **2016**, *28*, 9326.
[43] X. Li, A. Tang, J. Li, L. Guan, G. Dong, F. Teng, *Nanoscale Res. Lett.* **2016**, *11*, 171.
[44] M. Alam Khan, Y.-M. Kang, *J. Energy Storage* **2016**, *7*, 252.
[45] Y. Sun, F. Alimohammadi, D. Zhang, G. Guo, *Nano Lett.* **2017**, *17*, 1963.
[46] W. Jung, S. Lee, D. Yoo, S. Jeong, P. Miró, A. Kuc, T. Heine, J. Cheon, *J. Am. Chem. Soc.* **2015**, *137*, 7266.
[47] D. Sun, S. Feng, M. Terrones, R. E. Schaak, *Chem. Mater.* **2015**, *27*, 3167.
[48] Y. Sun, Y. Wang, D. Sun, B. R. Carvalho, C. G. Read, C. Lee, Z. Lin, K. Fujisawa, J. A. Robinson, V. H. Crespi, M. Terrones, R. E. Schaak, *Angew. Chem., Int. Ed.* **2016**, *55*, 2830.
[49] B. Mahler, V. Hoepfner, K. Liao, G. A. Ozin, *J. Am. Chem. Soc.* **2014**, *136*, 14121.
[50] D. Yoo, M. Kim, S. Jeong, J. Han, J. Cheon, *J. Am. Chem. Soc.* **2014**, *136*, 14670.
[51] S. Yang, C. Jiang, S. Wei, *Appl. Phys. Rev.* **2017**, *4*, 021304.
[52] Z. Yin, H. Li, H. Li, L. Jiang, Y. Shi, Y. Sun, G. Lu, Q. Zhang, X. Chen, H. Zhang, *ACS Nano* **2012**, *6*, 74.
[53] F. Xia, T. Mueller, Y. Lin, A. Valdes-Garcia, P. Avouris, *Nat. Nanotechnol.* **2009**, *4*, 839.
[54] Y. Zhou, E. Song, J. Zhou, J. Lin, R. Ma, Y. Wang, W. Qiu, R. Shen, K. Suenaga, Q. Liu, J. Wang, Z. Liu, J. Liu, *ACS Nano* **2018**, *12*, 4486.
[55] S. E. Hosseini, M. A. Wahid, *Renewable Sustainable Energy Rev.* **2016**, *57*, 850.
[56] J. A. Turner, *Science* **2004**, *305*, 972.
[57] I. Roger, M. A. Shipman, M. D. Symes, *Nat. Rev. Chem.* **2017**, *1*, 0003.
[58] S. Bellani, L. Najafi, A. Capasso, A. E. Del Rio Castillo, M. R. Antognazza, F. Bonaccorso, *J. Mater. Chem. A* **2017**, *5*, 4384.
[59] J. Yang, H. S. Shin, *J. Mater. Chem. A* **2014**, *2*, 5979.
[60] J. D. Benck, T. R. Hellstern, J. Kibsgaard, P. Chakthranont, T. F. Jaramillo, *ACS Catal.* **2014**, *4*, 3957.
[61] L. Najafi, S. Bellani, R. Oropesa-Nuñez, A. Ansaldo, M. Prato, A. E. Del Rio Castillo, F. Bonaccorso, *Adv. Energy Mater.* **2018**, *8*, 1703212.
[62] W. Xiao, P. Liu, J. Zhang, W. Song, Y. P. Feng, D. Gao, J. Ding, *Adv. Energy Mater.* **2017**, *7*, 1602086.
[63] L. Najafi, S. Bellani, R. Oropesa-Nuñez, A. Ansaldo, M. Prato, A. E. Del Rio Castillo, F. Bonaccorso, *Adv. Energy Mater.* **2018**, *8*, 1801764.
[64] J. Zhang, T. Wang, P. Liu, S. Liu, R. Dong, X. Zhuang, M. Chen, X. Feng, *Energy Environ. Sci.* **2016**, *9*, 2789.
[65] M. A. R. Anjum, H. Y. Jeong, M. H. Lee, H. S. Shin, J. S. Lee, *Adv. Mater.* **2018**, *30*, 1707105.
[66] J. Kibsgaard, Z. Chen, B. N. Reinecke, T. F. Jaramillo, *Nat. Mater.* **2012**, *11*, 963.
[67] D. Voiry, M. Salehi, R. Silva, T. Fujita, M. Chen, T. Asefa, V. B. Shenoy, G. Eda, M. Chhowalla, *Nano Lett.* **2013**, *13*, 6222.
[68] B. Hinnemann, P. G. Moses, J. Bonde, K. P. Jørgensen, J. H. Nielsen, S. Horch, I. Chorkendorff, J. K. Nørskov, *J. Am. Chem. Soc.* **2005**, *127*, 5308.
[69] Y. Yu, S.-Y. Huang, Y. Li, S. N. Steinmann, W. Yang, L. Cao, *Nano Lett.* **2014**, *14*, 553.
[70] Y. Jiao, A. M. Hafez, D. Cao, A. Mukhopadhyay, Y. Ma, H. Zhu, *Small* **2018**, *14*, 1800640.
[71] A. Ambrosi, Z. Sofer, M. Pumera, *Chem. Commun.* **2015**, *51*, 8450.
[72] T. F. Jaramillo, K. P. Jorgensen, J. Bonde, J. H. Nielsen, S. Horch, I. Chorkendorff, *Science* **2007**, *317*, 100.
[73] R. F. Bacon, E. S. Boe, *Ind. Eng. Chem.* **1945**, *37*, 469.
[74] D. Chen, Y. Gao, Y. Chen, Y. Ren, X. Peng, *Nano Lett.* **2015**, *15*, 4477.
[75] S. A. Dalmatova, A. D. Fedorenko, L. N. Mazalov, I. P. Asanov, A. Yu. Ledneva, M. S. Tarasenko, A. N. Enyashin, V. I. Zaikovskii, V. E. Fedorov, *Nanoscale* **2018**, *10*, 10232.
[76] C. Ronning, H. Feldermann, R. Merk, H. Hofsäss, P. Reinke, J.-U. Thiele, *Phys. Rev. B* **1998**, *58*, 2207.
[77] C. H. Ho, Y. S. Huang, K. K. Tiong, P. C. Liao, *Phys. Rev. B* **1998**, *58*, 16130.
[78] J. Tauc, *Mater. Res. Bull.* **1968**, *3*, 37.
[79] J. I. Pankove, D. A. Kiewit, *J. Electrochem. Soc.* **1972**, *119*, 156C.
[80] H. Liu, B. Xu, J.-M. Liu, J. Yin, F. Miao, C.-G. Duan, X. G. Wan, *Phys. Chem. Chem. Phys.* **2016**, *18*, 14222.
[81] N. R. Pradhan, A. McCreary, D. Rhodes, Z. Lu, S. Feng, E. Manousakis, D. Smirnov, R. Namburu, M. Dubey, A. R. Hight Walker, H. Terrones, M. Terrones, V. Dobrosavljevic, L. Balicas, *Nano Lett.* **2015**, *15*, 8377.
[82] A. McCreary, J. R. Simpson, Y. Wang, D. Rhodes, K. Fujisawa, L. Balicas, M. Dubey, V. H. Crespi, M. Terrones, A. R. Hight Walker, *Nano Lett.* **2017**, *17*, 5897.
[83] G. Gouadec, P. Colomban, *Prog. Cryst. Growth Charact. Mater.* **2007**, *53*, 1.
[84] W. Yang, L. Gan, H. Li, T. Zhai, *Inorg. Chem. Front.* **2016**, *3*, 433.
[85] X. Tang, A. Du, L. Kou, *Wiley Interdiscip. Rev.: Comput. Mol. Sci.* **2018**, *8*, e1361.
[86] P. R. Brown, D. Kim, R. R. Lunt, N. Zhao, M. G. Bawendi, J. C. Grossman, V. Bulović, *ACS Nano* **2014**, *8*, 5863.
[87] G. H. Carey, A. L. Abdelhady, Z. Ning, S. M. Thon, O. M. Bakr, E. H. Sargent, *Chem. Rev.* **2015**, *115*, 12732.
[88] D. J. Late, Y.-K. Huang, B. Liu, J. Acharya, S. N. Shirodkar, J. Luo, A. Yan, D. Charles, U. V. Waghmare, V. P. Dravid, C. N. R. Rao, *ACS Nano* **2013**, *7*, 4879.
[89] S.-Y. Cho, S. J. Kim, Y. Lee, J.-S. Kim, W.-B. Jung, H.-W. Yoo, J. Kim, H.-T. Jung, *ACS Nano* **2015**, *9*, 9314.
[90] E. Petroni, E. Lago, S. Bellani, D. W. Boukhvalov, A. Politano, B. Gürbulak, S. Duman, M. Prato, S. Gentiluomo, R. Oropesa-Nuñez, J.-K. Panda, P. S. Toth, A. E. Del Rio Castillo, V. Pellegrini, F. Bonaccorso, *Small* **2018**, *14*, 1800749.
[91] L. Najafi, S. Bellani, R. Oropesa-Nuñez, B. Martin-Garcia, M. Prato, V. Mazanek, D. Debellis, S. Laucello, R. Brescia, Z. Sofer, F. Bonaccorso, *J. Mater. Chem. A* **2019**, *7*, 25593.
[92] K. A. Mauritz, R. B. Moore, *Chem. Rev.* **2004**, *104*, 4535.
[93] P. S. Khadke, U. Krewer, *J. Phys. Chem. C* **2014**, *118*, 11215.
[94] K. Shinozaki, B. S. Pivovar, S. S. Kocha, *ECS Trans.* **2013**, *58*, 15.
[95] H.-C. Tu, W.-L. Wang, C.-C. Wan, Y.-Y. Wang, *J. Phys. Chem. B* **2006**, *110*, 15988.
[96] L. Najafi, S. Bellani, B. Martín-García, R. Oropesa-Nuñez, A. E. Del Rio Castillo, M. Prato, I. Moreels, F. Bonaccorso, *Chem. Mater.* **2017**, *29*, 5782.
[97] Q. Liu, Q. Fang, W. Chu, Y. Wan, X. Li, W. Xu, M. Habib, S. Tao, Y. Zhou, D. Liu, T. Xiang, A. Khalil, X. Wu, M. Chhowalla, P. M. Ajayan, L. Song, *Chem. Mater.* **2017**, *29*, 4738.
[98] M. Boudart, *Chem. Rev.* **1995**, *95*, 661.
[99] T. Shinagawa, A. T. Garcia-Esparza, K. Takanabe, *Sci. Rep.* **2015**, *5*, 13801.
[100] L. Najafi, S. Bellani, R. Oropesa-Nuñez, M. Prato, B. Martín-García, R. Brescia, F. Bonaccorso, *ACS Nano* **2019**, *13*, 3162.
[101] Y. Liu, J. Wu, K. P. Hackenberg, J. Zhang, Y. M. Wang, Y. Yang, K. Keyshar, J. Gu, T. Ogitsu, R. Vajtai, J. Lou, P. M. Ajayan, B. C. Wood, B. I. Yakobson, *Nat. Energy* **2017**, *2*, 17127.
[102] J. Zhang, J. Wu, X. Zou, K. Hackenberg, W. Zhou, W. Chen, J. Yuan, K. Keyshar, G. Gupta, A. Mohite, P. M. Ajayan, J. Lou, *Mater. Today* **2019**, *25*, 28.
[103] L. Najafi, S. Bellani, R. Oropesa-Nunez, B. Martin-Garcia, M. Prato, F. Bonaccorso, *ACS Appl. Energy Mater.* **2019**, *2*, 5373.

[104] J. Shi, X. Wang, S. Zhang, L. Xiao, Y. Huan, Y. Gong, Z. Zhang, Y. Li, X. Zhou, M. Hong, Q. Fang, Q. Zhang, X. Liu, L. Gu, Z. Liu, Y. Zhang, *Nat. Commun.* **2017**, *8*, 958.
[105] H. Li, C. Tsai, A. L. Koh, L. Cai, A. W. Contryman, A. H. Fragapane, J. Zhao, H. S. Han, H. C. Manoharan, F. Abild-Pedersen, J. K. Nørskov, X. Zheng, *Nat. Mater.* **2016**, *15*, 48.
[106] G. Ye, Y. Gong, J. Lin, B. Li, Y. He, S. T. Pantelides, W. Zhou, R. Vajtai, P. M. Ajayan, *Nano Lett.* **2016**, *16*, 1097.
[107] S. Bolar, S. Shit, J. S. Kumar, N. C. Murmu, R. S. Ganesh, H. Inokawa, T. Kuila, *Appl. Catal., B* **2019**, *254*, 432.
[108] L. Cheng, W. Huang, Q. Gong, C. Liu, Z. Liu, Y. Li, H. Dai, *Angew. Chem., Int. Ed.* **2014**, *53*, 7860.
[109] R. Zhang, X. Wang, S. Yu, T. Wen, X. Zhu, F. Yang, X. Sun, X. Wang, W. Hu, *Adv. Mater.* **2017**, *29*, 1605502.
[110] J. Deng, H. Li, S. Wang, D. Ding, M. Chen, C. Liu, Z. Tian, K. S. Novoselov, C. Ma, D. Deng, X. Bao, *Nat. Commun.* **2017**, *8*, 14430.
[111] Y. Li, H. Wang, L. Xie, Y. Liang, G. Hong, H. Dai, *J. Am. Chem. Soc.* **2011**, *133*, 7296.
[112] J. D. Holladay, J. Hu, D. L. King, Y. Wang, *Catal. Today* **2009**, *139*, 244.
[113] K. Zeng, D. Zhang, *Prog. Energy Combust. Sci.* **2010**, *36*, 307.
[114] F. Safizadeh, E. Ghali, G. Houlachi, *Int. J. Hydrogen Energy* **2015**, *40*, 256.
[115] I. Moussallem, J. Jörissen, U. Kunz, S. Pinnow, T. Turek, *J. Appl. Electrochem.* **2008**, *38*, 1177.
[116] D. Pletcher, X. Li, *Int. J. Hydrogen Energy* **2011**, *36*, 15089.
[117] M. Carmo, D. L. Fritz, J. Mergel, D. Stolten, *Int. J. Hydrogen Energy* **2013**, *38*, 4901.
[118] S. A. Grigoriev, V. I. Porembsky, V. N. Fateev, *Int. J. Hydrogen Energy* **2006**, *31*, 171.
[119] F. Qi, X. Wang, B. Zheng, Y. Chen, B. Yu, J. Zhou, J. He, P. Li, W. Zhang, Y. Li, *Electrochim. Acta* **2017**, *224*, 593.
[120] C. Gammer, C. Mangler, C. Rentenberger, H. P. Karnthaler, *Scr. Mater.* **2010**, *63*, 312.